

Modal analysis of photonic and plasmonic resonators: user guide for the MAN program

T. Wu^{1,†}, D. Arrivault¹, W. Yan^{2,3}, P. Lalanne^{1,*}

¹LP2N, Institut d'Optique Graduate School, CNRS, Univ. Bordeaux, 33400 Talence, France

²Key Laboratory of 3D Micro/Nano Fabrication and Characterization of Zhejiang Province, School of Engineering, Westlake University, 18 Shilongshan Road, Hangzhou 310024, Zhejiang Province, China

³Institute of Advanced Technology, Westlake Institute for Advanced Study, 18 Shilongshan Road, Hangzhou 310024, Zhejiang Province, China

* philippe.lalanne@institutoptique.fr

† wutong1121@gmail.com

Abstract

Any electromagnetic system, in particular resonators, has resonances with finite lifetimes. The associated eigenstates, also called quasinormal modes, are essentially non-Hermitian and determine optical responses of the system. We introduce **MAN** (**M**odal **A**nalysis of **N**anoresonators), a software with many open scripts which computes and normalizes the quasinormal modes of virtually any electromagnetic resonator, be it composed of dispersive, anisotropic, or non-reciprocal materials. **MAN** reconstructs the scattered field in the basis formed by the quasinormal modes of the resonator and provides a transparent interpretation of the physics.

The software is implemented in MATLAB and has been developed over the past ten years. **MAN** features many toolboxes that illustrate how to use the software for various emblematic computations in nanophotonics. A specific effort has been devoted to interface the solver with the finite-element software COMSOL Multiphysics. However, the software can also be used with other frequency-domain numerical solvers. This article introduces the program, summarizes the relevant theory, and is supplemented by a comprehensive suite of classic examples that can be downloaded from our web.

Program Summary

Program title: MAN

CPC Library link to program files: XXXXX

Licensing provisions: GNU General Public License 3

Developer's repository link: <https://www.lp2n.institutoptique.fr/equipes-de-recherche-du-lp2n/light-complex-nanostructures>

Programming language: Matlab, Comsol

Nature of problem: Compute and normalize the quasinormal-modes of optical resonators of any type, be it composed of dispersive, anisotropic, or non-reciprocal materials. Use the quasinormal-modes to reconstruct the optical responses: scattered field, local density of states, second-harmonic field, and so on.

Solution method: Two methods are offered. The quasi-normal modes are computed either by solving the linearized Maxwell's equation or searching poles in the complex frequency plane.

KEYWORDS: Computational electromagnetic methods, Resonators, Quasinormal mode, Microcavity devices, Nanoresonator, Inverse design, Plasmon.

1. Motivation

The interaction of light with electromagnetic resonators is fundamentally driven by the natural resonances of the system. Under excitation by a pulse, the resonances are initially loaded, and then release their energy by exponentially decaying in time. Resonators are open non-Hermitian systems that do not conserve their energy. This is why their supported resonances are often called *quasinormal modes* (QNMs), therein emphasizing that they are the eigenvectors of a non-Hermitian operator, the Maxwell operator, with complex eigenfrequencies. They are formally defined as the time-harmonic solutions to the source-free Maxwell equations [1]

$$\begin{aligned}\nabla \times \tilde{\mathbf{E}} &= -i\tilde{\omega}\mu(\mathbf{r}, \tilde{\omega})\tilde{\mathbf{H}}, \\ \nabla \times \tilde{\mathbf{H}} &= i\tilde{\omega}\epsilon(\mathbf{r}, \tilde{\omega})\tilde{\mathbf{E}},\end{aligned}\tag{1}$$

+ outgoing waves conditions at infinity.

We use the $\exp(i\omega t)$ convention and denote with a tilde QNM complex-valued frequencies, $\tilde{\omega} = \Omega + i\Gamma/2$, where Γ stands for the decay rate, i.e., the inverse of the mode lifetime $\tau = 1/\Gamma$. The factor $1/2$ accounts for the difference between amplitude and energy decays. Throughout the article, $[\tilde{\mathbf{E}}(\mathbf{r}), \tilde{\mathbf{H}}(\mathbf{r})]$ denotes the electric and magnetic fields of normalized QNMs. Normalization is central in QNM theory. It is not documented in the present article; for more informations, please refer to other sources, e.g. Sec. 4 in [2] that reviews and compares various methods to normalize QNMs.

In this work, we present **MAN** (**Modal Analysis of Nanoresonator**), an open-source software that uses the QNM basis for analyzing the response of virtually any micro or nanoresonators, be them photonic, plasmonic, or composed of non-reciprocal dispersive materials. **MAN** is the result of a collective effort, initiated at the Institut d'Optique in Palaiseau by Jean-Paul Hugonin, Christophe Sauvan and Philippe Lalanne [3,4] and continued in Bordeaux over the last decade [1,2,5-12].

MAN has two main purposes. First, it offers efficient ways to compute and normalize the QNMs by gathering the two first available freeware, **QNMPole** [3,4] and **QNMEig** [6] that were respectively launched in 2013 and 2018, in a user-friendly package implemented in MATLAB. Second, it provides various toolboxes for reconstructing the resonator responses, e.g. scattered field, extinction and absorption cross-sections, local density of electromagnetic states (LDOS), as a superposition of QNMs.

MAN is conceived to help the user to analyze the physics of electromagnetic resonators and identify the dominant QNMs to offer physical transparency in the design or interpretation. It devotes special attention to the computation of key QNM figures of merit, such as the mode volume, a complex quantity for non-Hermitian systems that is central to the notion of LDOS involved in the resonant interaction of light with molecules or atoms [1,11]. It also informs the user on important QNM properties, such as their far-field radiation pattern, their multipolar nature, or their brightness for absorptive resonators.

2. Underlying principles of the code

2.1. Overview

Figure 1 shows the structure of the software. The source code is composed of four main folders: *TUTORIALS*, *SOLVERS*, *TOOLBOXES*, and *DOC*, which are completed by a *+tests* folder for internal use by the software developers.

The *TUTORIALS* folder contains several MATLAB scripts, e.g. Tutorial2D.m and Tutorial3D.m, which provide a step-by-step guidance to help the user to compute, normalize, sort, and save the QNMs computed with the solvers **QNMEig** or **QNMPole**. See Section 2.2 for details.

The *SOLVER* folder contains all the MATLAB functions used by the QNM solvers and companion scripts for QNMs computation, postprocessing, and visualization.

The QNM solvers are valued by an increasing number of toolboxes gathered in the *TOOLBOXES* folder. The toolboxes contain illustrative examples and user guides of emblematic problems in

nanophotonics. A detailed introduction to the toolboxes is found in Sec. 4. The toolboxes are solver dependent; this is quite formal since, with a minor effort from the user, the toolboxes developed for one solver may be adapted for use with the other solver.

The *DOC* folder contains user guides for **QNMEig**, **QNMPole**, and all the toolboxes in **MAN**.

By executing the MATLAB `buildAndSaveComsolModels.m` script of the *TUTORIALS* folder, a new folder named *MANMODELS* will be created in the root folder of **MAN**. The *MANMODELS* folder is composed of over 20 COMSOL models, including photonic crystal cavities, plasmonic nanospheres, nano-particle-on-mirror (NPoM) geometries, and so on. Each model is solver-dependent. They can be studied with either **QNMEig** or **QNMPole**, but not with both solvers. The panel of models will grow up and develop over time.

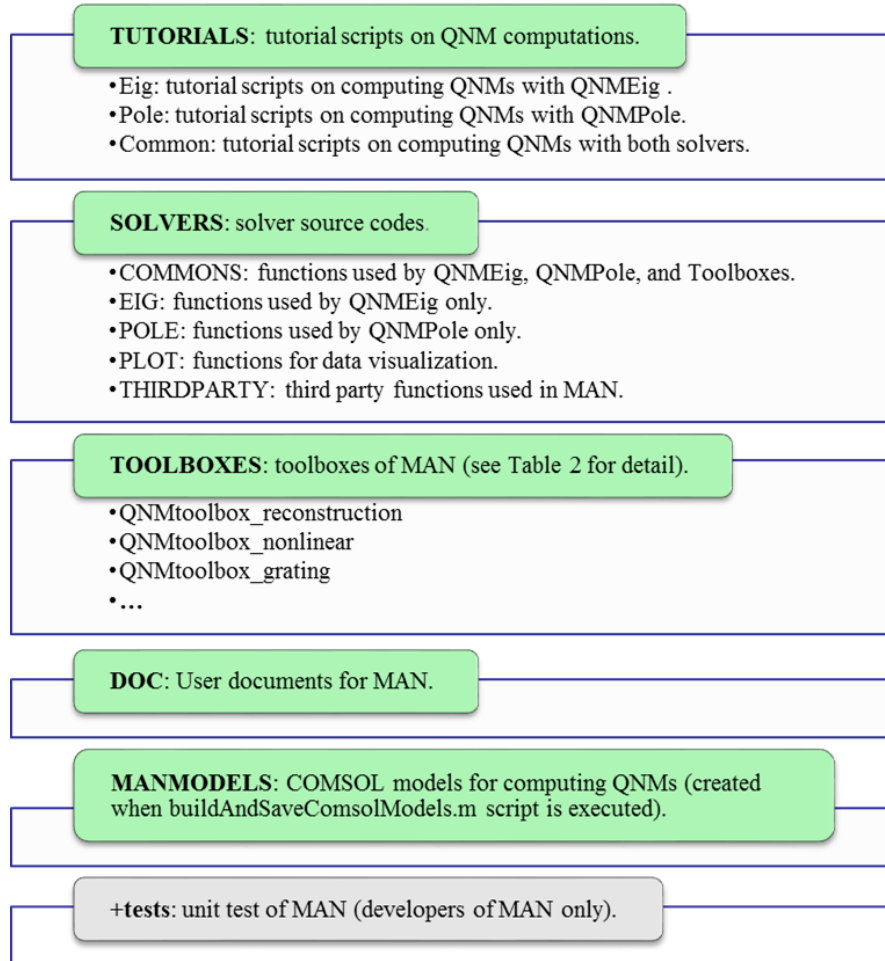


Fig. 1. Structure of **MAN**.

2.2. QNM solvers

To cover a broad scope of applications, **MAN** implements two largely different QNM solvers.

QNMEig can be viewed as an extension of the eigenmode solver implemented in the COMSOL Multiphysics RF Module. The RF Module eigenmode solver is effective and accurate only for QNMs of non-dispersive materials. For dispersive materials, the Maxwell operator defines a non-linear eigenproblem since the permittivity (or permeability) depends on the eigenvalue and the RF Module solver becomes inaccurate. **QNMEig** computes the QNMs by coupling the built-in RF Module and Weak-form Module. The solver linearizes the eigenproblem with auxiliary fields and efficiently computes a large number (assigned by the user) of QNMs with high accuracy [6], even for highly

dispersive media. The QNMs are then normalized by computing a volume integral with the so-called PML-normalization [2,3]. Sections 5.1 and 5.2 provide more details, see also [6]. Approximately 20 COMSOL models can be used with **QNMEig**. They cover many geometries and materials (see Table 1) of current interest in nanophotonics.

QNMPole computes and normalizes the QNMs by searching poles in the complex frequency plane [4], starting from an initial guess value and iteratively exploring the complex plane around the pole. Compared to **QNMEig**, **QNMPole** is more general, since it can be used for any material dispersion (Table 1). It also requires less computational skills than **QNMEig**, since the user does not have to linearize the eigenvalue problem with auxiliary fields. However, it is in general less efficient than **QNMEig**, since the QNMs have to be computed sequentially. The use of **QNMPole** is recommended to compute a few QNMs, or if the permittivities of some dispersive constitutive materials do not obey the Lorentz-Drude and N -pole Lorentz models. **QNMPole** in principle can be used with any software capable of solving Maxwell equations in the frequency domain. We have presently only provided an interface with the RF Module of COMSOL. The user has to supply the interface if they use other software. The documentation explains how to build the interface with MATLAB and how to enable computations at complex frequencies with a software initially restrained for operation at real frequencies, e.g. the RF module of COMSOL. For details, please refer to the user guide QNMPole V7.pdf in the *DOC/pdf/solvers/pole* folder.

Table 1. Summary of the QNMEig and QNMPole solvers.

Solver	QNM computation method	Constitutive materials	Companion software needed
QNMEig [6]	Auxiliary fields for solving a linearized version of the eigenvalue problem.	<u>Lorentz-Drude:</u> $\varepsilon(\omega)/\varepsilon_\infty = 1 - \sum_{n=1}^N \omega_{pn}^2 / (\omega^2 - \omega_{0n}^2 - i\omega\gamma_n)$. <u>N-pole Lorentz:</u> $\varepsilon(\omega) = 1 + \sum_{n=1}^N [A_n / (\omega - \omega_n) - A_n^* / (\omega + \omega_n^*)]$. <u>Constant tensor.</u>	<ul style="list-style-type: none"> • COMSOL Multiphysics RF Module • COMSOL Multiphysics Weak-form Module • MATLAB (for postprocessing and data visualization)
QNMPole [4]	Iterative pole search in the complex frequency plane.	Any permittivity or permeability with a frequency dependence that is analytically known.	<ul style="list-style-type: none"> • Any software solving Maxwell equations in the frequency domain. • MATLAB (for driving Maxwell solvers to search poles, postprocessing, and data visualization)

Note that **QNMPole** and **QNMEig** strictly provide the same eigenfrequencies and normalized QNMs if they are both used with the same mesh.

2.3. QNM expansion

QNM expansion consists in decomposing the optical response as a sum of QNM contributions. It is central in any resonator analysis and is implemented in several toolboxes of **MAN**, e.g. the *reconstruction*, *non-linear*, *grating* toolboxes (see Section 4 for details).

The literature distinguishes two classes of methods to expand the response (i.e., the field $\mathbf{E}_S(\mathbf{r}, \omega)$ scattered by the resonator excited by a monochromatic driving field at frequency ω) into a sum of QNM contributions, see Table 1 in Ref. [2].

The residue-expansion method exploits the fact that, under certain conditions, a representative function of the system response (often its Green's tensor) is a meromorphic function that can be decomposed as a sum of its poles (Mittag-Leffler theorem), which are the QNMs [13]. Completeness of the QNM expansion of the scattered field, $[\mathbf{E}_S(\mathbf{r}, \omega), \mathbf{H}_S(\mathbf{r}, \omega)] = \sum_m \alpha_m(\omega) [\tilde{\mathbf{E}}_m(\mathbf{r}), \tilde{\mathbf{H}}_m(\mathbf{r})]$, is

achieved for a subspace of \mathbb{R}^3 (inside the resonator) only for resonators surrounded by a uniform background (no substrate) [2].

In the second method adopted in **MAN**, the continuous Maxwell operator, originally defined on an open space, is replaced by a discretized linear operator, with a bounded physical domain surrounded by perfectly matched layers (PMLs) [14]. The latter transforms the open space into a regularized Hilbert space [2,6,15], replacing the exponential growth of the QNM field in the open space by an exponential decay in the PMLs. The regularized eigenvectors of the discretized operator are composed of a finite subset of the true QNMs $[\tilde{\mathbf{E}}_m(\mathbf{r}), \tilde{\mathbf{H}}_m(\mathbf{r})]$ of the open system (typically the subset includes the dominant resonances driving the resonator response) and a large subset of numerical modes (sometimes called PML modes [15]), which originates from the finite-discretized space bounded by PMLs [2,6]. The QNM expansion

$$\begin{bmatrix} \mathbf{E}_S(\mathbf{r}, \omega) \\ \mathbf{H}_S(\mathbf{r}, \omega) \end{bmatrix} = \sum_{m=1 \dots \infty} \alpha_m(\omega) \begin{bmatrix} \tilde{\mathbf{E}}_m(\mathbf{r}) \\ \tilde{\mathbf{H}}_m(\mathbf{r}) \end{bmatrix} + \sum_{p=1 \dots \infty} \alpha_p^{num}(\omega) \begin{bmatrix} \tilde{\mathbf{E}}_p^{num}(\mathbf{r}) \\ \tilde{\mathbf{H}}_p^{num}(\mathbf{r}) \end{bmatrix}, \quad (2)$$

is complete for all \mathbf{r} of the regularized (numerical) space, including the PMLs (see Section 5.3 for detail). In Eq. (2), the numerical modes $[\tilde{\mathbf{E}}_p^{num}(\mathbf{r}), \tilde{\mathbf{H}}_p^{num}(\mathbf{r})]^T$ are denoted just like the true QNMs, by simply adding a superscript ‘num’ for the sake of differentiation. They are computed exactly as the true QNMs, by solving the source-free Maxwell equations of Eq. (1).

The dependence of the excitation coefficients, α_m or α_p^{num} , with the driving field is analytical, as will be highlighted in Sections 4.2.1 and 4.2.2. This implies that, once the eigenvectors are computed and normalized, the reconstruction of the scattered field for many instances of the driving field becomes trivial, even in the temporal domain for resonators illuminated by pulses (see Section 4.3).

The true QNMs and the numerical modes are treated in **MAN** in exactly the same way; they are computed with the same solvers, and their excitation coefficients obey the same closed-form expression. In fact, mathematically, it is therefore not necessary to distinguish them, and we will abusively refer to both types of eigenvectors as QNMs, hereafter.

3. Getting started

3.1. Installation

To install MAN, one simply needs to unzip MAN-8.zip, then starts COMSOL Multiphysics with MATLAB, and adds the path of the main directory as well as the paths of all subfolders to the MATLAB search path. To do it, the user may run the function *addManPath.m* in the main directory:

```
>> addManPath;
```

MAN incorporates more than 20 COMSOL models with various geometries and materials. They can be helpful to the users to create their own models. When using **MAN** for the first time, start by running *buildAndSaveComsolModels.m* in the *TUTORIALS* folder:

```
>> buildAndSaveComsolModels;
```

This will create a new folder named *MANMODELS* in the root directory of **MAN**. *MANMODELS* contains all the COMSOL models (‘.mph’ files). The user will find two kinds of models with filenames started with ‘QNMEig’ and ‘QNMPole’, respectively

The QNMEig models can be used with the **QNMEig** solver. They can be run independently of any MATLAB script in **MAN** if the user goal is just to compute the normalized QNMs. Together with the models, we have provided several documents (click Sphere, Cubesubstrate, ... in the MAN User Guide.html file in the *DOC* folder) explaining how these COMSOL models are built. Special attention has been paid to explain how to handle dispersive media by coupling the COMSOL RF and Weak-form Modules. Note that depending on whether the permittivity (or permeability by a straightforward extension) of the dispersive constitutive materials is described by Drude-Lorentz or N-Pole Lorentz functions, the formulas entered in the Weak-form Module are different. The documents Sphere,

Cubesubstrate, ... provide the procedures to deal with the Drude-Lorentz permittivity. The user may refer to the model QNMEig_NanolettSi.mph for an example of a N-Pole Lorentz permittivity.

The QNMPole models can be used with the **QNMPole** solver. In contrast to **QNMEig** files, these models need to be operated by a MATLAB script to compute and normalize the QNMs by iteratively searching for poles in the complex frequency plane [4]. The building of these QNMPole models is fairly easy, as they are very similar to the COMSOL models used for simulating the scattered field of the resonator at real frequency.

The users are encouraged to build their own models by modifying the existing examples that are provided.

3.2. Initial step: tutorial

For a quick start, please start with one of the examples of the *TUTORIALS* folder, e.g. Tutorial2D.m, Tutorial3D.m, which provides a step-by-step illustration of how to compute, normalize, sort, and visualize QNMs using **QNMEig** or **QNMPole**. These examples may help understand the toolboxes that will be described in Section 4 to inspire the user to develop their own applications.

Let us just consider the script Tutorial2D.m dedicated to 2D problems. A similar script, Tutorial3D.m, exists for 3D. Tutorial2D.m computes the TE or TM supermodes of a pair of silicon nanowires. The computation can be performed by using either **QNMEig** or **QNMPole**.

```
>>mansolver = 'eig'; or >>mansolver = 'pole';
```

Then, the user should choose a model in a predefined list (obtained by calling get2DEigModelList or get2DPoleModelList) or should build their own model. The MATLAB script either drives COMSOL to compute the QNMs or loads the precomputed results if the models in the folder *MANMODELS* are used. In general, the computation of the QNMs will consume most of the computer time. To save time for further use, we strongly recommend that the user save their model into a COMSOL file in *MANMODELS* after the first computation by calling

```
>> [mphfile,mphfolder] = saveModel(Model);
```

Hence, the QNMs do not have to be recomputed and can be loaded by calling

```
>> QNM = getEigQNMs(Model);
```

3.3. Minimal example

Once the QNMs are computed or loaded, the next step is to determine the QNMs of interest. Important information about the QNMs is displayed using the function plotComplexPlane:

```
>> plotComplexPlane(Model,QNM);
```

Figure 2 displays the MATLAB figure generated by the function, showing the position of the complex eigenfrequencies of all the computed eigenstates in the complex frequency plane. In general, the user is first interested in identifying the dominant QNMs that drive the physics of their systems. It is often a tedious task, and MAN helps the user by introducing two figures of merit:

- the mode ratio ($MR \in [0,1]$, see the MAN User Guide.html in the *DOC* folder for the precise definition) shown by the disk color of every eigenvalue, which indicates the likelihood that the eigenstate is a true QNM ($MR = 1$, yellow) or a numerical mode ($MR = 0$, blue);
- the excitation strength ($ES \in [0,1]$, see the MAN User Guide.html for the precise definition) shown by the disk size of every eigenvalue, which characterizes the likelihood that the mode is excited by a plane wave.

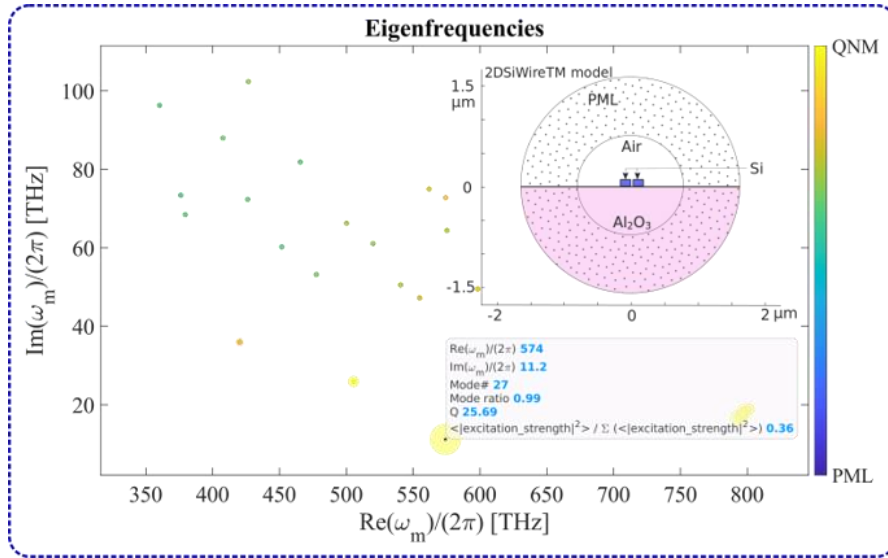


Fig. 2. Complex frequency plane and QNM information for a coupled pair of 2D silicon nanowires displayed with the function `plotComplexPlane`. The size and color of the markers visualize the excitation strength and mode ratio, respectively. Other important information about the QNMs can be shown by clicking the mode in the figure. Inset: Sketch of the nanowire pair.

Finally, it is possible to load the QNM near fields and permittivities in any user-defined coordinates by calling the functions,

```
>> QNM = getModalFields(Model, QNM, 'coord', coord);
>> permitt = getRelativePermittivity(Model, QNM, coord);
```

and plot maps of the QNM fields and the permittivity.

4. Toolboxes

4.1 Overview

Table 2 lists the toolboxes of the Version 8. New toolboxes may be added in future versions for other applications. This section provides a short introduction to the toolboxes content; a step-by-step presentation can be found in the user guide documents inside the *DOC* folder.

Table 2. List of the toolboxes in MAN. (*) denotes the toolboxes released for the first time in Version 8.

Toolbox acronym (Year of first release)	Further reading	Description
<i>reconstruction</i> (*) (2022)	[3,4,6]	Compute the QNM excitation coefficients α . Reconstruct the electromagnetic fields, absorption and extinction cross-sections, Purcell factors, and LDOS using QNMs.
<i>alpha-coefficient</i> (2019)	[6]	Same as for the reconstruction toolbox, but only valid for the simplest case where the resonator embedded in free space is excited with a plane wave.
<i>nonreciprocal</i> (2021)	[11,12]	Compute and normalize QNMs for nonreciprocal resonators.
<i>nonlinear</i> (2020)	[9]	Solve nonlinear response of nanoresonators (second-harmonic generation) in the QNM basis.
<i>grating</i> (2019)	[7]	Compute the specular reflection of 1D grating using QNM expansions.

<i>far-field-radiation</i> (*) (2022)	[11,16]	Generate the far-field radiation diagrams of QNMs.
<i>multipole</i> (2020)	[8]	Compute the intrinsic multipole moments of QNMs for resonators in free space.
<i>interpolation</i> (2021)	[10]	Provide a fast and accurate reconstruction of the resonator response by interpolating the non-resonant contribution at real frequency.
<i>temporal-domain</i> (*) (2022)	[5,6]	Reconstruct the temporal response of the resonator using QNMs.
<i>axisymmetric</i> (*) (2022)		Same as the reconstruction toolbox, but valid for optical resonators with axial symmetry.

Toolbox organization. Each toolbox can be found in a separate folder, which is composed of a user guide document and several dedicated MATLAB source codes. Since most toolboxes rely on general MATLAB functions in the *SOLVER* folder to generate figures and load QNM fields and other information from COMSOL models, this folder should be added to the MATLAB path before using the toolboxes.

The toolboxes use the COMSOL models of *MANMODELS* for computing the QNMs. To study other optical systems, new COMSOL models should be implemented by the user. Since the toolboxes often rely on parameters defined in the COMSOL models, e.g. the parameters of the Drude-Lorentz functions, the background permittivity, and domain numbers of the resonator, we recommend that the user follows the instruction of *MAN User Guide.html* to build their own models for accurate access to these parameters.

Caution. The toolboxes have been developed over different periods; their level of development may differ. For example, in the *reconstruction* toolbox, the user only needs to provide the angle of the incident plane wave and the background layered medium, and the background field inside the resonator (required to further compute the QNM excitation coefficients) is automatically computed. In the *nonlinear* toolbox, an analytical formula has to be provided for the background field inside the resonator. When starting with **MAN**, it is advised to study the code examples that are provided and follow them to develop a new application. Similar to the tutorial scripts, e.g. *Tutorial2D.m* or *Tutorial3D.m*, the example codes of the toolboxes also aim at giving pedagogical presentations that help the user to develop their own applications.

4.2 Near-field reconstruction in the frequency domain

In the *reconstruction* and the *alpha-coefficient* toolboxes, the reconstruction is performed with the QNM expansion of Eq. (2) over the regularized space, including the PMLs. If all the eigenvectors are considered in the expansion, the reconstruction is exact, in the sense that the reconstructed field obtained with a sum of QNM contributions is mathematically equal to the field computed with a real frequency solver with the same mesh [6].

An important question is how fast one approaches the exact result by increasing the number N of QNMs retained in the expansion. We may be interested in two kinds of convergence speed: asymptotic behaviors as $N \rightarrow \infty$ or initial behaviors on the accuracy achieved with only a few dominant QNMs (typically $N < 10$) that govern the physics of the system. The first kind of convergence is more mathematically directed, and the second kind is very important in practice. So far, the whole literature provides no clear answer to the questions of the convergence issues. Only a few numerical studies have been performed from case to case. State-of-the-art studies of the convergence performance for landmark plasmonic resonators can be found in Ref. [6]. Other interesting cases can be found in Refs. [7,15,17-19].

The convergence issue is also complicated due to the existence of an infinite number of rigorous formulas for the α_m 's (or α_p^{num} 's) for dispersive materials. The non-uniqueness arises from subtleties when choosing the source term with auxiliary fields, see Ref. [19] for details. Close to the resonance frequency ($\tilde{\omega}_m \rightarrow \omega$), all the formulas converge to the same value, see Section 4.2 in [1]. However,

away from the resonance, the formulas give rise to significantly different values of α_m 's. We believe that the choice of the source term has a weak impact on the asymptotic convergence rate. However, it has an impact on the accuracy achieved for small N 's.

Over the past five years, we have studied this accuracy for various nanoresonator geometries. Depending on the geometry, we observe either very similar [19] or markedly different reconstruction accuracies [8,9]. We could not establish general rules, and this is the reason why special attention has been devoted to the implementation of the *reconstruction* toolbox. Overall, the latter offers a quite complete overview of the main methods available for reconstructing the near fields. In general terms, we recommend that the user follows the approach in [6] (method **M 1** hereafter). Then, if they are not satisfied with the convergence or accuracy, they may try the other methods, especially method **M 2** that helped us much in our recent works [8,9].

The *reconstruction* and *alpha-coefficient* toolboxes also compute useful optical responses, e.g. the extinction and absorption cross-sections, and the Purcell factors. Note that, in contrast with the *reconstruction* toolbox, the *alpha-coefficient* toolbox is valid only for resonators in free space and does not reconstruct the near-field. The later can be viewed as a simplified version of the former that may have a better practicality for resonator in uniform media (without substrate).

4.2.1 QNM excitation coefficient

For non-dispersive materials, there is a unique expression for the α_m 's (or α_p^{num} 's) [4,19]

$$\alpha_m(\omega) = \iiint_{V_{res}} \left(\Delta\epsilon(\mathbf{r}, \omega) \frac{\omega}{\tilde{\omega}_m - \omega} \right) \mathbf{E}_b \cdot \tilde{\mathbf{E}}_m d^3\mathbf{r}, \quad (3)$$

where $\Delta\epsilon(\mathbf{r}, \omega) = \epsilon(\mathbf{r}, \omega) - \epsilon_b$ is the permittivity difference defining the resonator volume V_{res} in the scattering field formulation, see Annex 2 in Ref. [1] for details, and \mathbf{E}_b is the background field (the driving field computed for $\Delta\epsilon = 0$). Note that a ω -dependence is included in $\Delta\epsilon(\mathbf{r}, \omega)$ in Eq. (3) to account for the fact that the expression is also valid for dispersive materials.

For resonators with Drude, multi-pole Drude-Lorentz, or multi-pole Lorentz permittivities, a classical and well-documented expression is [6]

$$\alpha_m(\omega) = \iiint_{V_{res}} \left(\epsilon_b(\mathbf{r}, \omega) - \epsilon_\infty(\mathbf{r}) + \Delta\epsilon(\mathbf{r}, \tilde{\omega}_m) \frac{\tilde{\omega}_m}{\tilde{\omega}_m - \omega} \right) \mathbf{E}_b \cdot \tilde{\mathbf{E}}_m d^3\mathbf{r}, \quad (4)$$

where $\epsilon_b(\mathbf{r}, \omega)$ is the background permittivity and $\epsilon_\infty(\mathbf{r})$ is the permittivity $\epsilon(\mathbf{r}, \omega \rightarrow \infty)$. Note that for non-dispersive materials, Eq. (3) and Eq. (4) are identical. $\epsilon_b(\mathbf{r}, \omega)$ does not necessarily correspond to a homogeneous medium. It may correspond to a layered substrate, as illustrated in Fig. 3. Then, the background field \mathbf{E}_b is composed of counterpropagating plane waves that are reflected and transmitted in the layers under illumination by the incident field. \mathbf{E}_b can be computed with 2×2 matrix products for isotropic materials; this computation is automatically performed by the *reconstruction* toolbox provided that the user defines the background permittivities and the incident plane-wave parameters as explained in .

According to our experience, the formulas of Eqs. (3) and (4) provide similar convergence performance when reconstructing the total field using the methods in Table 3.

Expressions for α_m 's also exist for resonators driven by localized sources, such as localized sources with an electric dipole \mathbf{p} or magnetic dipole \mathbf{m} moments located at a position \mathbf{r}_0 in the near field. An infinity of expressions may also be derived for dispersive resonators; however, in contrast to the plane wave case, the whole literature seems to have adopted the convenient (fully analytical) expression [3,11]

$$\alpha_m^{(t)}(\omega) = \frac{\omega}{\tilde{\omega}_m - \omega} [\mathbf{p} \cdot \tilde{\mathbf{E}}_m(\mathbf{r}_0, \tilde{\omega}_m) - \mathbf{m} \cdot \tilde{\mathbf{B}}_m(\mathbf{r}_0, \tilde{\omega}_m)], \quad (5)$$

for the total field $[\mathbf{E}_{tot}(\mathbf{r}, \omega), \mathbf{H}_{tot}(\mathbf{r}, \omega)] = \sum_m \alpha_m^{(t)}(\omega) [\tilde{\mathbf{E}}_m(\mathbf{r}), \tilde{\mathbf{H}}_m(\mathbf{r})]$, see also the discussion in Section 5.2 in [1]. The *reconstruction* toolbox implements this expression only.

4.2.2 Field reconstruction

To illustrate the possibilities offered by the *reconstruction* toolbox, consider the representative system shown in Fig. 3. The system is composed of five domains corresponding to five different materials. The background is composed of three domains, labeled 2, 3, and 4. The resonator is composed of two other domains. We assume that only the materials of domains 1 and 4 are dispersive.

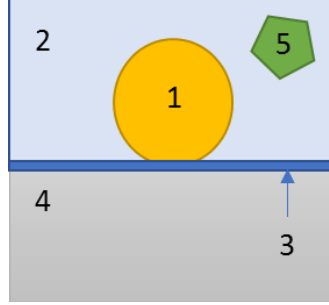


Fig. 3. Illustrative example of a system suited for simulation with the *reconstruction* toolbox. The background is defined by a multilayer structure (domains 2, 3, 4). The resonator is defined by the two other domains, 1 and 5. Only the materials of domains 1 and 4 are dispersive.

The QNMs have different field components, and each component can be used for the reconstruction of the total electric field \mathbf{E}_{tot} (see Section 5.4 for details). The *reconstruction* toolbox implements 2×4 different methods (labeled **M 1**, **M 2**, **M 3**, and **M 4** in Table 3) to reconstruct \mathbf{E}_{tot} for illumination by a plane wave. The factor 2 accounts for the fact that two different equations for the α_m 's can be used for each method. The methods have been selected for their accuracy, simplicity, or broad use.

For all methods, the reconstruction in the non-dispersive domains (2, 3, 5 in the example) is always performed with

$$[\mathbf{E}_{tot}(\mathbf{r}, \omega), \mathbf{H}_{tot}(\mathbf{r}, \omega)] = [\mathbf{E}_b(\mathbf{r}, \omega), \mathbf{H}_b(\mathbf{r}, \omega)] + \sum_m \alpha_m(\omega) [\tilde{\mathbf{E}}_m(\mathbf{r}), \tilde{\mathbf{H}}_m(\mathbf{r})], \quad (6)$$

$\alpha_m(\omega)$ being given either Eq. (3) or Eq. (4). The methods differ only for the dispersive domains, 1 and 4.

Table 3. A summary of important formulas implemented in the *reconstruction* toolbox for reconstructing the total field, \mathbf{E}_{tot} , in dispersive domains. Four methods (**M 1-M 4**) are considered, and each may rely on two different formulas for the α_m 's.

α_m	Eq. (4)		Eq. (3)	
Dispersive Dom. n^0	1 (resonator)	4 (background)	1 (resonator)	4 (background)
M 1	$\sum \alpha_m(\omega) \tilde{\mathbf{E}}_m + \mathbf{E}_b$			
M 2	$\sum \alpha_m(\omega) \frac{\varepsilon(\tilde{\omega}_m) - \varepsilon_\infty}{\varepsilon(\omega) - \varepsilon_\infty} \tilde{\mathbf{E}}_m$	$\sum \alpha_m(\omega) \frac{\varepsilon(\tilde{\omega}_m) - \varepsilon_\infty}{\varepsilon(\omega) - \varepsilon_\infty} \tilde{\mathbf{E}}_m + \mathbf{E}_b$		
M 3	$\sum \alpha_m(\omega) \frac{\varepsilon(\tilde{\omega}_m) - \varepsilon_\infty}{\varepsilon(\omega) - \varepsilon_\infty} \frac{\tilde{\omega}_m}{\omega} \tilde{\mathbf{E}}_m$	$\sum \alpha_m(\omega) \frac{\varepsilon(\tilde{\omega}_m) - \varepsilon_\infty}{\varepsilon(\omega) - \varepsilon_\infty} \frac{\tilde{\omega}_m}{\omega} \tilde{\mathbf{E}}_m + \mathbf{E}_b$		
M 4	$\sum \alpha_m(\omega) \frac{\varepsilon(\tilde{\omega}_m)}{\varepsilon(\omega)} \frac{\tilde{\omega}_m}{\omega} \tilde{\mathbf{E}}_m + \frac{\varepsilon_b(\omega)}{\varepsilon(\omega)} \mathbf{E}_b$			

All the methods asymptotically converge towards the same value if all the eigenvectors are included in the expansion. However, for small truncation ranks, they may provide significantly different accuracies. Figure 4 illustrates our purpose for a simple plasmonic system, a Dolmen composed of three Drude silver nanorods embedded in an air background. The response of the Dolmen at optical

frequencies is dominated by four QNMs shown in Fig. 4(b). Figure 4(c) shows the reconstruction performed with methods **M 1-4** and $\alpha_m(\omega)$ computed with Eq. (4) for a wavelength of 700 nm. They are obtained for an incident field polarized along the x -direction, $\mathbf{E}_b = -\mathbf{e}_x \exp(ik_b z)$, and are compared with Fig. 4(d) that displays the full-wave frequency simulated result obtained with COMSOL. For the reconstruction inside the dolmen, methods **M 2-M 4** are more accurate compared to the most intuitive method **M 1**. We have also observed a faster convergence of **M 2-M 4** for other nanostructures, such as a Si nanocylinder on a low refractive index substrate [9]. We refer the readers to Section 5.4 for a possible explanation of the faster convergence of **M 2-M 4** when reconstructing with a small set of QNMs.

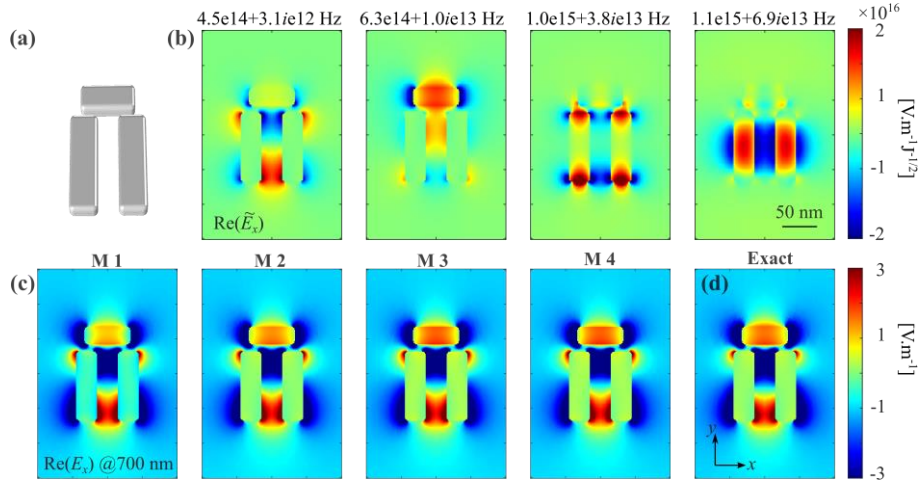


Fig 4. QNM reconstruction of the real part of the electric field, $\text{Re}(E_x)$, for a Dolmen-like structure. (a) The plasmonic dolmen is made of silver and composed of an upper rod ($66 \times 26 \times 20 \text{ nm}^3$) separated by a gap of width $g = 10 \text{ nm}$ from two lower rods ($30 \times 100 \times 20 \text{ nm}^3$) separated by 30 nm. The silver permittivity of the nanorods is approximated by a single-pole Drude model with $\varepsilon_\infty = 1$, $\omega_p = 1.366 \times 10^{16} \text{ rad}$, and $\gamma = 0.0023\omega_p$. The dolmen is embedded in air ($\varepsilon_b = 1$). (b) Electric field x -component $\text{Re}(\tilde{E}_x)$ in xy -plane of the four dominant QNMs used in the reconstruction. (c) Real part of the scattered electric fields $\text{Re}(E_x)$ for $\lambda = 700 \text{ nm}$ reconstructed with methods **M 1-M 4**. The incident field is a plane wave polarized along the x -direction. (d) $\text{Re}(E_x)$ obtained with fully vectorial numerical computations. The user is encouraged to repeat the figure by running QNMToolbox_reconstruction_Dolmen2.m in the *TOOLBOXES* folder.

4.2.3 Extinction and scattering cross-sections, Purcell factor

In the *reconstruction* and *alpha-coefficient* toolboxes, the extinction and scattering cross-sections, σ_{Ext} and σ_{Abs} , are accurately computed with the following formulas [4]

$$\sigma_{Ext} = -\frac{\omega}{2I_0} \iiint_{V_{res}} \text{Im}[\Delta\varepsilon(\omega)\mathbf{E}_{tot} \cdot \mathbf{E}_b^*] dV, \quad (7)$$

and

$$\sigma_{Abs} = -\frac{\omega}{2I_0} \iiint_{V_{res}} \text{Im}[\varepsilon(\omega)] |\mathbf{E}_{tot}|^2 dV, \quad (8)$$

where I_0 is the time averaging Poynting vector of the incident plane wave. The scattering cross section is then deduced with the difference $\sigma_{Sca} = \sigma_{Ext} - \sigma_{Abs}$.

Since multiple methods can be used for the reconstruction of \mathbf{E}_{tot} , an equal number of expressions for σ_{Ext} and σ_{Abs} that give different results for truncated expansions are available. The *reconstruction* toolbox implements time-tested expressions in our previous papers [4,6].

For dispersive resonators and provided that the α_m 's are computed with Eq. (4), we use the formulas derived in Ref. [6]. The $\Delta\varepsilon(\omega)\mathbf{E}_{tot}$ term in σ_{Ext} , Eq. (7), is decomposed into two terms:

$\Delta\epsilon(\mathbf{r}, \omega)\mathbf{E}_{tot} = (\epsilon_\infty - \epsilon_b)\mathbf{E}_{tot} + (\epsilon(\omega) - \epsilon_\infty)\mathbf{E}_{tot}$. We use **M 1** (resp. **M 3**) in Table 3 to reconstruct \mathbf{E}_{tot} in the first (resp. second) term. For σ_{Abs} , we use **M 3** to reconstruct \mathbf{E}_{tot} . These formulas may benefit from the fact that **M 3** may offer a faster convergence as compared to **M 1** when considering a small set of QNMs. For non-dispersive resonators, the α_m 's are obtained with Eq. (3), σ_{Ext} and σ_{Abs} are obtained by reconstructing \mathbf{E}_{tot} with method **M 1** [4].

Table 4 summarizes the formulas for computing σ_{Ext} and σ_{Abs} with the *reconstruction* toolbox.

Table 4. A summary of important formulas implemented in the *reconstruction* toolbox for reconstructing the extinction and absorption cross-sections.

	α_m 's computed with Eq. (3)	α_m 's computed with Eq. (4)
σ_{Ext}	$-\frac{\omega}{2I_0} \iiint_{V_{res}} \text{Im}[\Delta\epsilon(\omega)] \left(\sum \alpha_m \tilde{\mathbf{E}}_m + \mathbf{E}_b \right) \cdot \mathbf{E}_b^* dV$	$\iiint_{V_{res}} -\text{Im} \left[\sum [\epsilon(\tilde{\omega}_m) - \epsilon_\infty] \tilde{\omega}_m + [\epsilon_\infty - \epsilon_b] \omega \right] \alpha_m \frac{\tilde{\mathbf{E}}_m \cdot \mathbf{E}_b^*}{2I_0} dV$
σ_{Abs}	$-\frac{\omega}{2I_0} \iiint_{V_{res}} \text{Im}[\epsilon(\omega)] \left \sum \alpha_m \tilde{\mathbf{E}}_m + \mathbf{E}_b \right ^2 dV$	$-\frac{\omega}{2I_0} \iiint_{V_{res}} \text{Im}[\epsilon(\omega)] \left \sum \alpha_m \frac{\epsilon(\tilde{\omega}_m) - \epsilon_\infty}{\epsilon(\omega) - \epsilon_\infty} \frac{\tilde{\omega}_m}{\omega} \tilde{\mathbf{E}}_m \right ^2 dV$

Figures 5(a-b) show examples of results obtained with the *reconstruction* toolbox for a silver nanocube antenna on a gold substrate, separated by an 8 nm thick polymer spacer. The geometrical and material parameters are found in Fig 5(a). The antenna is illuminated with a plane wave for an incidence angle $\theta_i = 55^\circ$. We adopt Eq. (4) to compute the α_m 's. As the antenna materials are dispersive, the *reconstruction* toolbox automatically selects the formulas of the second column of Table 4 to compute σ_{Ext} and σ_{Abs} . The blue (extinction) and red (absorption) curves are obtained by considering two QNMs.. For the sake of comparison, we also show reference data (circles) obtained with the frequency-domain solver of COMSOL. The agreement is quantitative over the entire spectrum.

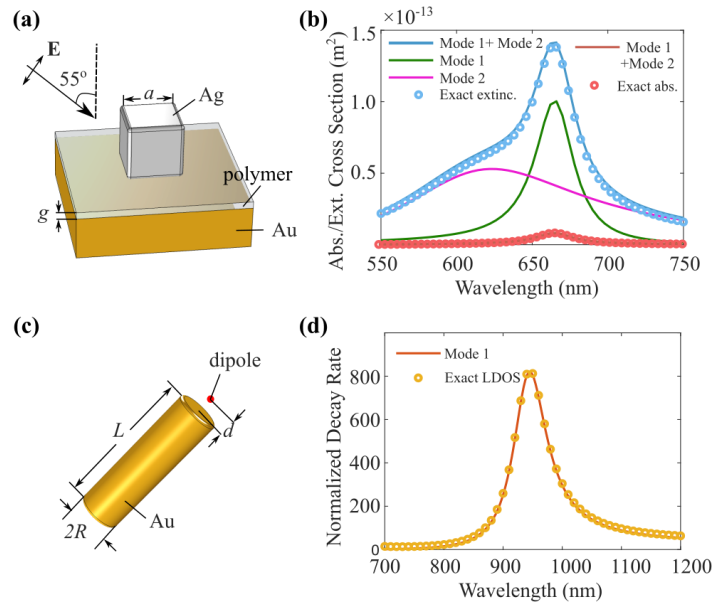


Fig. 5. Some well-converged examples of reconstruction in the QNM basis for very small N 's. (a) Schematic representation of an Ag nanocube antenna of size $a = 65$ nm deposited on a 8-nm-thick polymer film (refractive index $n = 1.5$) coated on an Au substrate. The incident wave is an oblique TM-polarized plane wave. (b) Cross-section spectra (solid blue and red curves) reconstructed with 2 QNMs and compared with reference 'exact' data (circles) computed with COMSOL. (c) An Au nanorod ($L = 65$ nm, $R = 15$ nm) is embedded in a host medium of refractive index $n = 1.5$. (d) Normalized decay-rate spectrum for an on-axis dipole oriented parallel to the nanorod (red dot) and located at a distance $d = 10$ nm. The Ag permittivity is found in the caption of Fig. 4. For gold, we use a double pole Drude–Lorentz model with $\epsilon_\infty = 6$, $\omega_{p1} = 5.37 \times$

10^{15} rad , $\gamma_1 = 6.22 \times 10^{13}$ rad , $\omega_{01} = 0$ rad , $\omega_{p2} = 2.26 \times 10^{15}$ rad , $\omega_{02} = 4.57 \times 10^{15}$ rad, and $\gamma_2 = 1.33 \times 10^{15}$ rad. The user is encouraged to repeat the figures by running QNMToolbox_reconstruction_NPoM_cube.m and QNMToolbox_reconstruction_rod_dipole.m in the *TOOLBOXES* folder.

The *reconstruction* toolbox also incorporates functions that allow to compute the Purcell factor P_m and normalized LDOS (γ/γ_0), when a resonator is driven by electric \mathbf{p} or magnetic \mathbf{m} dipoles (or a Dirac source with both moments) [3,11]

$$\frac{\gamma}{\gamma_0} = \sum_m P_m = -\frac{2}{\hbar\gamma_0} \sum_m \text{Im} \left[\alpha_m^{(t)} (\mathbf{p}^* \cdot \tilde{\mathbf{E}}_m(\mathbf{r}_0) + \mathbf{m}^* \cdot \tilde{\mathbf{B}}_m(\mathbf{r}_0)) \right], \quad (9)$$

where the excitation coefficient $\alpha_m^{(t)}$ is computed using Eq. (5) and $\gamma_0 = \omega^3 [|\mathbf{p}|^2 + |\mathbf{m}|^2/c^2]/(3\pi\epsilon_0\hbar c^3)$ denotes the vacuum spontaneous decay rate.

Figure 5 (c-d) illustrates a simple problem, a gold nanorod driven by an electric dipole emitter oriented parallel to the nanorod axis, for which the Purcell factor is accurately computed with a single QNM in the expansion [4]. Using the classical frequency-domain solver of COMSOL, we first compute the normalized LDOS according to the definition: $\frac{\gamma}{\gamma_0} = -\frac{2}{\hbar\gamma_0} \text{Im}[\mathbf{p}^* \cdot \mathbf{E}_{tot}(\mathbf{r}_0)]$. We then reconstruct the LDOS using Eq. (9). The result reconstructed by considering only the longitudinal electric dipole antenna QNM is shown with the red line.

Figure 5 provide two examples for which the optical response can be accurately reconstructed with a very few number of QNMs. In practice, there also exist systems, e.g. resonators on substrates supporting guiding modes, dipole emitters placed very close to metal surfaces and quenched, and low Q resonators, where a large set of QNMs have to be incorporated to achieve an accurate reconstruction [6]. However, we do not recommend the user to compute a large number of QNMs, as it is time consuming. Rather we recommend to compute the few QNMs that capture the main resonant feature of the spectrum, and use the *interpolation* toolbox (see Section 4.9) to obtain an accurate reconstruction with a small amount of computational loads.

4.3 Reconstruction in the temporal domain

The study of the dynamics of optical nanoresonators under irradiance by a pulsed beam is indispensable for analyzing ultrafast optical phenomena and nonlinear light-matter interactions [20]. To obtain insights into the physics of the temporal responses, the analysis is best performed in the QNM basis, see Fig. 6.

The *temporal-domain* toolbox takes advantage of the ω – analyticity of the frequency-domain expansion of Eq. (2) to effectively compute the temporal responses of optical nanoresonators in the QNM basis by applying a temporal ($\omega \leftrightarrow t$) Fourier transformation (FT)

$$[\mathbf{E}_S(\mathbf{r}, t), \mathbf{H}_S(\mathbf{r}, t)] = \text{Re} \left(\sum_m \beta_m(t) [\tilde{\mathbf{E}}_m(\mathbf{r}), \tilde{\mathbf{H}}_m(\mathbf{r})] \right), \quad (10)$$

with $\beta_m(t)$ the time-dependent modal excitation coefficient given by

$$\beta_m(t) = \text{FT}[\alpha_m(\omega)]. \quad (11)$$

In the toolbox, by default, the temporal intensity profile of the incident wave has a Gaussian shape, and the spatial profile is a plane wave. The parameters of the pulsed light, including central frequency, pulse duration, propagation direction and polarization, are set by the user. Two different β_m 's are computed from Eqs. (3) [5] and (4) [6].

For resonators that can be modeled with a few QNMs, the temporal QNM reconstruction can be extremely advantageous in terms of computational loads. Indeed, once the QNMs are known, the incident pulse duration, polarization or incidence angle can be changed at will since the reconstruction just relies on a 1D Fourier transform, which can be evaluated in a few seconds. In contrast, with the FDTD, any new instance of the driving field requires a new computation. Additionally, the knowledge

of the individual contribution of each QNM in the temporal responses significantly helps in interpreting the physics. These two decisive advantages are illustrated in Fig. 6 for a dolmen-type nanoresonator composed of three gold nanorods. The literature on temporal QNM reconstruction in nanophotonics is scarce; an advanced example of reconstruction with an analysis of the kind of shape that can be obtained for $\beta_m(t)$ can be found in [6].

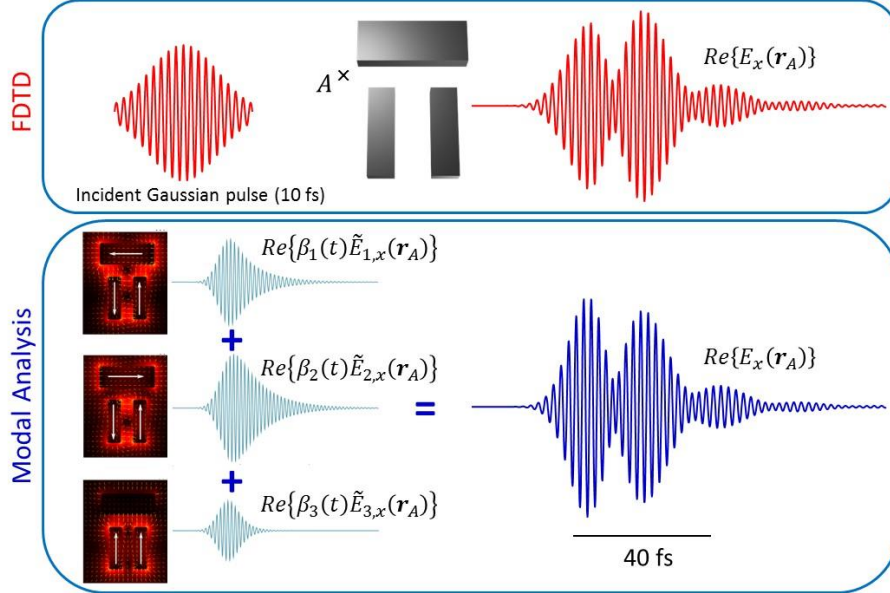


Fig. 6. Analysis of the temporal response of nanoresonators with QNM expansions. A dolmen-type nanoresonator is illuminated by a 10 fs plane-wave Gaussian pulse with a central frequency $\omega_0 = 2.9 \times 10^{15}$ rad/s. Its near-field response at point A , as predicted with the FDTD (red), is faithfully reconstructed and explained as resulting from the beating of three dominant QNMs. The dolmen example and the comparison between the FDTD data and the 3-QNM reconstruction are further analyzed in Ref. [5].

4.4 QNM far-field radiation

The QNMEig and QNMPole solvers compute the near-field pattern of normalized QNMs. For many applications, it is also interesting to know the QNM contribution to the far-field radiation.

The far-field is easily computed by applying a near-to-far-field transformation (NFFT), which computes radiation diagrams. We may symbolically write

$$\text{NFFT}_\omega[\mathbf{E}_S(\mathbf{r}, \omega), \mathbf{H}_S(\mathbf{r}, \omega)] = \sum_m \alpha_m(\omega) \text{NFFT}_\omega[\tilde{\mathbf{E}}_m(\mathbf{r}), \tilde{\mathbf{H}}_m(\mathbf{r})]. \quad (12)$$

As shown in Fig. 4d in [6], the reconstruction of the field scattered in the far-field with Eq. (12) is very accurate. Theoretically, the near-to-far-field transform depends on the frequency of interest ω , and this is the reason why we add a subscript ω to NFFT in Eq. (12). This implies that one should perform a new near-to-far-field transform to know the far-field radiation at each new frequency, say $\omega' \neq \omega$. This may be demanding in computational resources.

To reduce the number of computations, the toolbox performs the near-to-far-field transform for each QNM at its own frequency $\text{Re}(\tilde{\omega}_m)$; the far field then reads as

$$\text{NFFT}_\omega[\mathbf{E}_S(\mathbf{r}, \omega), \mathbf{H}_S(\mathbf{r}, \omega)] \approx \sum_m \alpha_m(\omega) \text{NFFT}_{\text{Re}(\tilde{\omega}_m)}[\tilde{\mathbf{E}}_m(\mathbf{r}), \tilde{\mathbf{H}}_m(\mathbf{r})], \quad (13)$$

and $\text{NFFT}_{\text{Re}(\tilde{\omega}_m)}[\tilde{\mathbf{E}}_m(\mathbf{r}), \tilde{\mathbf{H}}_m(\mathbf{r})]$ becomes a quantity that is intrinsic to the QNM and that is computed once and for all. Equation (13) is approximate; it is accurate only if the QNMs with a resonance frequency $\tilde{\omega}_m \approx \omega$ are considered in the expansion.

The build-in near-to-far-field transform of COMSOL Multiphysics is valid only for objects surrounded by uniform media (free space). Thus, we recommend that the user downloads [21] and installs the

freeware RETOP [16] before using the toolbox. RETOP operates for objects on substrates or buried in stratified media and computes the radiation diagram in the superstrate and substrate. When the substrate supports guided modes or surface plasmon modes, RETOP additionally computes the in-plane radiation diagram of the guided modes.

The knowledge of the far-field radiated by a QNM is useful in practice. For instance, when an excited molecule dominantly decays into a bright QNM, an important question that arises is how the nanoresonator redirects the emitted light in the far-field or which numerical aperture is needed to collect most of the radiated light. This is central to access QNM brightness [11] and even optimize nanoresonator geometries to enhance the brightness through inverse design.

Note that the approximation made by computing the near-to-far-field transform at $\text{Re}(\tilde{\omega}_m)$ in Eq. (13) can be removed [22].

4.5 Multipole expansion

Interference between multipole moments of photonic or plasmonic nanoresonators is known to lead to many exotic phenomena, like zero forward or backward scattering, non-radiating anapole responses, and Fano resonances [23,24]. A standard approach to analyze the multipolar response of a resonator consists in expanding the scattered field upon a specific excitation into spherical harmonics [25]. The multipole analysis is thus performed for a particular instance of the driving field (wavelength, incident direction, and polarization) it is not intrinsic to the resonator and does not give any insight into the resonator properties at other wavelengths.

In contrast, the *multipole* toolbox analyzes the multipolar content of QNMs at complex frequencies. It provides transparent physics since the multipolar content becomes an intrinsic property of the resonance, irrespectively of the illumination condition. This markedly changes design perspectives toward operation over a broad range of frequencies or incidence angles or both [8].

The multipolar decomposition at complex frequencies implemented in the toolbox is analogous to the decomposition performed at real frequencies [25]. When the resonator is immersed in a homogenous medium with a refractive index n_b , the multipolar content of a QNM is determined by expanding its electric field $\tilde{\mathbf{E}}$ in vector spherical wave functions (VSWFs) [8]

$$\tilde{\mathbf{E}}(\mathbf{r}) = \tilde{k}^2 \sum_{n=1}^{\infty} \sum_{m=-n}^n E_{nm} \left[\tilde{a}_{nm} \tilde{\mathbf{N}}_{nm}^{(3)}(\mathbf{r}, \tilde{\omega}) + \tilde{b}_{nm} \tilde{\mathbf{M}}_{nm}^{(3)}(\mathbf{r}, \tilde{\omega}) \right], \quad (14)$$

where \tilde{a}_{nm} and \tilde{b}_{nm} are electric and magnetic multipole coefficients, $\tilde{\mathbf{N}}_{nm}^{(3)}(\mathbf{r}, \tilde{\omega})$ and $\tilde{\mathbf{M}}_{nm}^{(3)}(\mathbf{r}, \tilde{\omega})$ are the outgoing VSWFs and $\tilde{k} = \tilde{\omega}/c$ is the complex wavevector of QNM. The *Multipole* toolbox computes the coefficients \tilde{a}_{nm} and \tilde{b}_{nm} by performing an inner product between the QNM field and the vector spherical wave functions (VSWFs) on a sphere surface circumscribing the resonator (see Fig. 7(a)). The Cartesian multipole moments of the QNM, electric dipole $\tilde{\mathbf{p}}$, magnetic dipole $\tilde{\mathbf{m}}$, and electric quadrupole $\tilde{\mathbf{Q}}^e$, can then be retrieved by matching their far-field expressions with those of the VSWFs in spherical coordinates [8,23]. The relation between the Cartesian multipole moments and the VSWF coefficients can be found in Ref. [8].

Figure 7(b) shows the example proposed in the toolbox, which may be reproduced by running the MATLAB script `main_field_multipole.m`. The Dolmen (same structure as Fig. 4) is designed so that \tilde{p}_x and \tilde{m}_z/c dominantly respond, have similar amplitudes, and are out of phase by approximately 90° (blue and red represent the real and imaginary parts) to implement a Janus response [8].

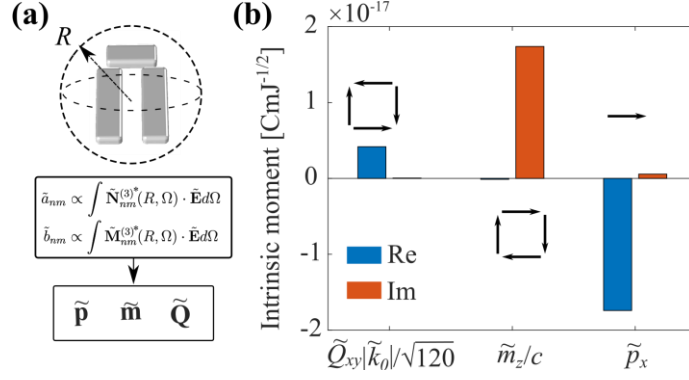


Fig. 7. (a) The *multipole* toolbox computes the coefficients \tilde{a}_{nm} and \tilde{b}_{nm} by performing an inner product between the QNM field and the vector spherical wave functions (VSWFs). **(b)** Multipole content of a Dolmen QNM provided by the *multipole* toolbox. The QNM is composed of electric and magnetic dipole moments, \tilde{p}_x and \tilde{m}_z , which have similar amplitudes and are out of phase by $\approx 90^\circ$ (Janus particle). The electric quadrupole component, \tilde{Q}_{xy} , is real and three time smaller.

4.6 Non-reciprocal materials

Non-reciprocal materials are usually found in magneto-optical materials biased by an external magnetic field. They are characterized by non-symmetric permeability or permittivity tensors, $\boldsymbol{\mu} \neq \boldsymbol{\mu}^T$ or $\boldsymbol{\varepsilon} \neq \boldsymbol{\varepsilon}^T$. The orthonormalization of QNMs deserves specific attention [2,11,12,26] in this case. It requires computing a left QNM, $\tilde{\mathbf{E}}_n^{(L)}$, which can be found by solving the eigenvectors of the source-free Maxwell operator with transposed permeability and permittivity, $\boldsymbol{\varepsilon}^T$ and $\boldsymbol{\mu}^T$. Note that, for nonreciprocal systems, the left $[\tilde{\mathbf{E}}_n^{(L)}, \tilde{\mathbf{H}}_n^{(L)}]$ and right $[\tilde{\mathbf{E}}_n^{(R)}, \tilde{\mathbf{H}}_n^{(R)}]$ QNMs differ: $\tilde{\mathbf{H}}_n^{(L)} \neq \tilde{\mathbf{H}}_n^{(R)}$ and $\tilde{\mathbf{E}}_n^{(L)} \neq \tilde{\mathbf{E}}_n^{(R)}$ (the right QNMs are the eigenvectors discussed in all other sections obtained for $\boldsymbol{\varepsilon}$ and $\boldsymbol{\mu}$ tensors). However, the left and right QNMs share the same eigenvalues, $\tilde{\omega}_n^{(R)} = \tilde{\omega}_n^{(L)} \equiv \tilde{\omega}_n$.

The expression of the QNM norm QN_n for non-reciprocal systems is [2,11,12]

$$QN_n = \iiint_{\Omega \cup \Omega_{\text{PML}}} \tilde{\mathbf{E}}_n^{(L)} \cdot \frac{\partial(\omega \boldsymbol{\varepsilon})}{\partial \omega} \tilde{\mathbf{E}}_n^{(R)} - \tilde{\mathbf{H}}_n^{(L)} \cdot \frac{\partial(\omega \boldsymbol{\mu})}{\partial \omega} \tilde{\mathbf{H}}_n^{(R)} dV, \quad (15)$$

where the integral is performed in the PML layer Ω_{PML} and the physical space Ω . Similarly, the mode volume reads as

$$\tilde{V}_n(\mathbf{r}, \mathbf{u}) = \left[2\varepsilon_0 \left(\tilde{\mathbf{E}}_n^{(L)} \cdot \mathbf{u} \right) \left(\tilde{\mathbf{E}}_n^{(R)} \cdot \mathbf{u} \right) / QN_n \right]^{-1}, \quad (16)$$

\mathbf{u} being the unit vector defining the polarization direction. For a derivation of these formulas and the related orthogonality condition, the reader may refer to Ref. [2] and the documentation of the *nonreciprocal_resonators* toolbox [12]. The latter presents a COMSOL model of a didactical example for computing and normalizing the non-reciprocal QNMs of a 2D yttrium-iron garnet wire in air. In this example, $\tilde{\mathbf{E}}_n^{(L)}$ and $\tilde{\mathbf{E}}_n^{(R)}$ largely differs, see Fig. 8 of [2]. Therefore, to compute QN_n or $\tilde{V}_n(\mathbf{r}, \mathbf{u})$, the eigensolver should be called twice.

4.7 Nonlinear nanophononics

The *nonlinear* toolbox illustrates a generic example of how to perform a QNM analysis of a second-harmonic generation with localized resonances in the small-signal regime. It promotes important nonlinear concepts such as mode overlap, field enhancement, and phase matching between ω and 2ω signals.

With the small-signal approximation, the pump depletion can be neglected, and the second-harmonic generation is described via two coherent processes. Under excitation by an external pump beam $\mathbf{E}_b(\mathbf{r}, \omega)$, a total field distribution $\mathbf{E}_{\text{tot}}(\mathbf{r}, \omega)$ is generated at the fundamental frequency ω . It

further induces a local nonlinear current inside the resonator, $\mathbf{J}^{(2)}(\mathbf{r}, 2\omega)$, which acts as the source for the second-harmonic radiation at 2ω .

In the *nonlinear* toolbox, the total field $\mathbf{E}_{tot}(\mathbf{r}, \omega)$ is expanded using Eq. (4) and **M 2** in Table 3. The nonlinear displacement current, $\mathbf{J}^{(2)}(\mathbf{r}, 2\omega)$, is then derived from the second-order nonlinear susceptibility $\chi^{(2)}$ and the total field $\mathbf{E}_{tot}^{(2)}(\mathbf{r}, 2\omega)$ generated at 2ω is reconstructed in the QNM basis $\mathbf{E}_{tot}^{(2)}(\mathbf{r}, 2\omega) = \sum_m \alpha_m^{(2)}(2\omega) \tilde{\mathbf{E}}_m(\mathbf{r})$. The analytically known modal coefficients $\alpha_m^{(2)}(2\omega)$ are computed by performing overlap integrals between the QNMs and the nonlinear current $\mathbf{J}^{(2)}(\mathbf{r}, 2\omega)$. Finally, from the knowledge of $\mathbf{E}_{tot}^{(2)}(\mathbf{r}, 2\omega)$, the nonlinear extinction cross-section $\sigma_{ext}^{(2)}(2\omega)$, a classical figure of merit defined as the ratio between the generated power at 2ω and the intensity of the incident field, is derived.

In the *nonlinear* toolbox, the second-harmonic generation is presented for an AlGaAs nanocylinder on a glass substrate [9]. The generic example may help the reader to implement other geometries or nonlinear processes.

4.8 Grating analysis and band diagram of crystal

Grating spectra exhibit sharp variations of the scattered light, known as grating anomalies or resonances, which are used in many applications. Using the example of a 1D periodic grating illuminated by a plane wave at oblique incidence, the *grating* toolbox illustrates how to compute and normalize the QNMs of periodic structures, to reconstruct the scattered field in the QNM basis.

In many works [15,27,28], the QNMs are defined for a fixed in-plane (parallel to the x -direction in Fig. 8) Bloch-wavevector \mathbf{k}_p . \mathbf{k}_p -QNMs are relevant for computing band diagrams but are irrelevant for analyzing grating spectra [7].

What sets the specificity of the *grating* toolbox is that it considers resonances that are effectively revealed by any experimental grating spectra measured for fixed incident angles. The resonances are QNMs obtained for a fixed angle of incidence ($\boldsymbol{\eta}$ -QNMs), i.e. a fixed “directionality” vector $\boldsymbol{\eta} = n_{inc} \sin \theta \hat{\mathbf{x}}$. $\boldsymbol{\eta}$ is a real vector that depends on the incident angle θ and the refractive index n_{inc} of the incident medium, but not on the frequency ω . \mathbf{k}_p - and $\boldsymbol{\eta}$ -QNMs are intrinsically different and have distinct normalizations [7]. Similarly, in a sensing experiment, the shift in resonance frequency is due to a perturbation of $\boldsymbol{\eta}$ -QNMs, not \mathbf{k}_p -QNMs, except if, unlikely, one records the spectra by simultaneously tuning the angle of incidence for every frequency of measurement.

The normalization of a $\boldsymbol{\eta}$ -QNM requires computing two QNMs: one with a “directionality” vector $\boldsymbol{\eta}$ and another one with another “directionality” vector $-\boldsymbol{\eta}$, see Fig. 8. The $-\boldsymbol{\eta}$ -QNM should be computed numerically, except if the grating has a mirror symmetry with respect to the vertical axis y , in which case, it can be deduced analytically from the $\boldsymbol{\eta}$ -QNM.

Figure 8 illustrates one of the few reconstructions available in the literature with $\boldsymbol{\eta}$ -QNMs [7].

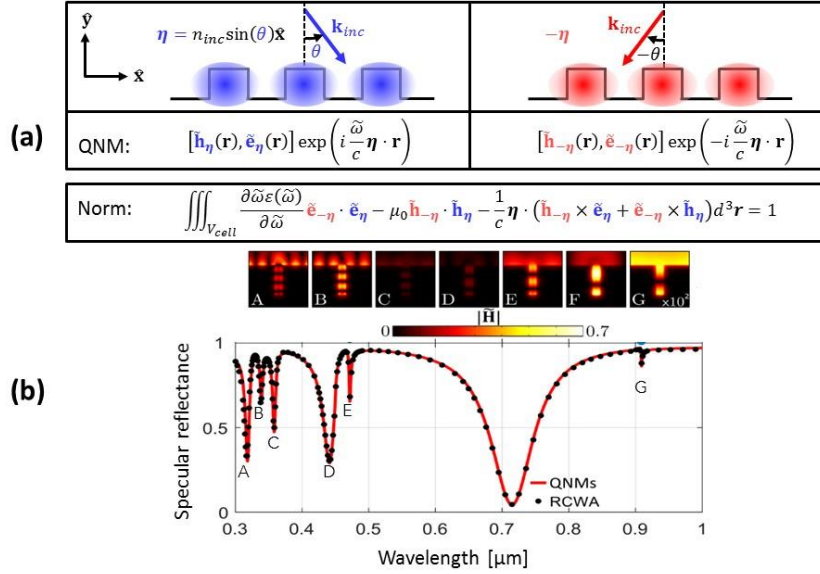


Fig. 8. *grating* toolbox. (a) The normalization of η -QNMs with a fixed “directionality” vector η relies on two reciprocal QNMs with “directionality” vectors η and $-\eta$. (b) Reconstruction of the reflectance spectrum of a gold lamellar grating illuminated by a TM-polarized plane wave ($\theta = 30^\circ$). The reconstructed spectrum obtained with 200 modes is compared with reference data obtained with the RCWA [28]. The upper inset shows the magnetic-field moduli of the seven dominant QNMs, labeled A, B, ... G. More details are found in the documentation and in [19].

4.9 Effective reconstruction with interpolation

Accurate reconstructions often require considering a large set of QNMs in the expansion in addition to the dominant QNMs of physical significance. For instance, it is systematically the case when the background is not uniform, since branch cuts, modeled as many individual poles, may then significantly contribute to the reconstruction [2,6]. The computation of all these poles (often referred to as numerical modes [2] or ‘PML modes’ [15]) is usually time-consuming and significantly dilutes the force of the modal approach.

The *interpolation* toolbox implements a simple approach to get around the necessity to consider the numerical modes. It relies on the ansatz that the numerical modes gently contribute to the reconstruction in the spectral range of interest: either their quality factors are extremely small (< 1) or their frequencies lie outside the spectral window of interest. The *interpolation* toolbox illustrates how to efficiently interpolate the smooth contribution with only a few (< 10) real frequency simulations, to reconstruct the scattered field as a combination of two contributions, that of the few dominant QNMs and that interpolated.

In this way, the physics of the resonator is made transparent and a fast computation with high accuracy is achieved; in general, the computation is much faster than those required with purely real frequency or temporal analysis [10].

5. Theoretical and numerical issues

5.1 The QNMPole and QNMEig solvers

QNMPole solver. **QNMPole** computes and normalizes the QNMs by an iterative procedure that computes poles following a Padé approximation [4]. The field $\mathbf{E}_S(\mathbf{r}, \omega)$ scattered by a resonator under excitation by a monochromatic field at frequency ω can be expanded as a superposition of its QNMs and numerical modes, see Eq. (2), and the excitation coefficient $\alpha_m(\omega)$ is proportional to $(\omega - \tilde{\omega}_m)^{-1}$ for first-order poles. This implies that the poles are the same for all \mathbf{r} .

The iterative procedure focuses on one of the scattered field components, e.g. the z-component $E_{Sz}(\mathbf{r}_0)$, at a fixed position \mathbf{r}_0 . It starts by considering three guessed frequencies, ω_1 , ω_2 and ω_3 , that are provided by the user and are slightly different from the searched pole and computes the three associated fields, $E_{Sz}(\omega_1)$, $E_{Sz}(\omega_2)$, $E_{Sz}(\omega_3)$. From this initial step, a new frequency, $\omega_4 = f(\omega_1, \omega_2, \omega_3, E_{Sz}(\omega_1), E_{Sz}(\omega_2), E_{Sz}(\omega_3))$, is automatically generated using the Padé approximation and the field $E_{Sz}(\omega_4)$ at frequency ω_4 is computed. The function f is given by Eq. (20) in Ref. [4]. The iterative procedure then starts. $f(\omega_2, \omega_3, \omega_4, E_{Sz}(\omega_2), E_{Sz}(\omega_3), E_{Sz}(\omega_4))$ is used to compute ω_5 . As the iteration number increases, $E_z(\omega_n)$ diverges and ω_n rapidly tends toward the eigenfrequency $\tilde{\omega}$. The convergence is usually achieved in about 5 iteration steps, see Fig. 9, provided that the initial values ω_1 , ω_2 and ω_3 are close enough from the pole.

Thus, **QNMPole** requires a frequency-domain solver that solves Maxwell equations at complex frequencies. Commercial softwares, e.g. the COMSOL RF Module, are retained to real frequencies in general. The documentation `userguide_QNMPole_V7.pdf` explains how to easily modify the permittivities and permeabilities of the system to trick the solver by artificially implementing complex frequencies with real ones.

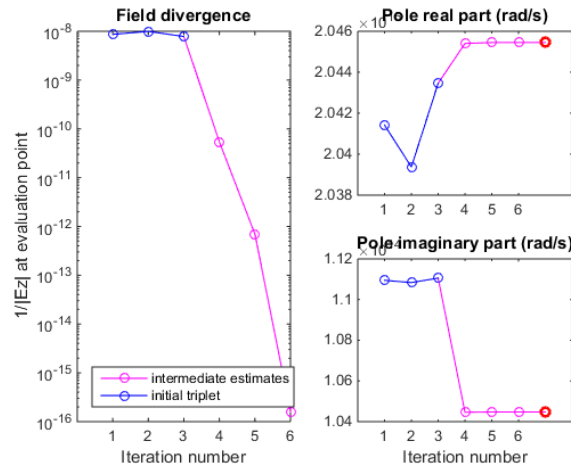


Fig. 9. Typical convergence observed with the **QNMPole**. The three guessed frequencies are labeled with blue circles. Further iterations are represented with pink circles. Left inset: Inverse of the scattered field computed at every iteration at the evaluation point; the inverse value should decrease by several orders of magnitude to guarantee convergence as one approaches the pole $\tilde{\omega}$. (right): Convergence of $\text{Re}(\omega_n)$ and $\text{Im}(\omega_n)$ as one approaches the pole. A plateau is already observed for the first iteration.

QNMEig solver. **QNMEig** extends the existing possibilities of the eigenmode solver of the COMSOL Multiphysics RF Module. It solves a quadratic eigenvalue problem of Maxwell's equations and handles materials with a Lorentz-Drude or N -pole Lorentz dispersions (see Table 1) using the auxiliary-field method [6,29-31]. These dispersions encompass many cases of interest in nanophotonics. Other types of dispersion can be implemented by the user following the linearization procedure implemented in **QNMEig**. For illustrating the procedure [6], let us consider the case of a material with a Lorentz-Drude dispersion $\varepsilon(\omega)/\varepsilon_\infty = 1 - \sum_{i=1}^N \frac{\omega_{p,i}^2}{\omega^2 - \omega_{0,i}^2 - i\omega\gamma_i}$. The quadratic eigenvalue formulation of the QNM reads as

$$\hat{\mathbf{R}}\mathbf{u} + \tilde{\omega}\hat{\mathbf{C}}\mathbf{u} + \tilde{\omega}^2\hat{\mathbf{M}}\mathbf{u} = \mathbf{0}. \quad (17)$$

Equation (17) formally corresponds to the Lorentz oscillator model. In the terminology of the finite-element method, $\hat{\mathbf{R}}$, $\hat{\mathbf{C}}$ and $\hat{\mathbf{M}}$ are the so-called stiffness, damping, and mass matrices, respectively

$$\hat{\mathbf{K}} = \begin{bmatrix} \nabla \times \mu_0^{-1} \nabla \times & 0 & 0 & \dots \\ \varepsilon_\infty \omega_{p,1}^2 & -\omega_{0,1}^2 & 0 & \dots \\ \varepsilon \omega_{p,2}^2 & 0 & -\omega_{0,2}^2 & \dots \\ \vdots & \vdots & \vdots & \ddots \end{bmatrix}, \quad (18)$$

$$\hat{\mathbf{C}} = \begin{bmatrix} 0 & 0 & 0 & \dots \\ 0 & -i\gamma_1 & 0 & \dots \\ 0 & 0 & -i\gamma_2 & \dots \\ \vdots & \vdots & \vdots & \ddots \end{bmatrix}, \quad (19)$$

$$\hat{\mathbf{M}} = \begin{bmatrix} -\varepsilon_\infty & -1 & -1 & \dots \\ 0 & 1 & 0 & \dots \\ 0 & 0 & 1 & \dots \\ \vdots & \vdots & \vdots & \ddots \end{bmatrix}. \quad (20)$$

In Eq. (17), \mathbf{u} is the augmented field vector,

$$\mathbf{u} = [\tilde{\mathbf{E}} \quad \tilde{\mathbf{P}}_1 \quad \tilde{\mathbf{P}}_2 \quad \dots], \quad (21)$$

which includes the electric field $\tilde{\mathbf{E}}$ and the introduced auxiliary polarization fields $\tilde{\mathbf{P}}_i$ ($\tilde{\mathbf{P}}_i \equiv -\varepsilon_\infty \frac{\omega_{p,i}^2}{\tilde{\omega}^2 - \omega_{0,i}^2 - i\tilde{\omega}\gamma_i} \tilde{\mathbf{E}}$).

The validity of Eq. (17) can be checked by replacing $\tilde{\mathbf{P}}_i$ with its definition in terms of $\tilde{\mathbf{E}}$ to obtain the Helmholtz equation. Equation (17) is fully compatible with the COMSOL eigenmode solver that solves quadratic eigenproblems with a remarkable efficiency through the so-called first companion linearization

$$\begin{bmatrix} \hat{\mathbf{K}} & \hat{\mathbf{C}} \\ \mathbf{0} & \mathbf{1} \end{bmatrix} \begin{bmatrix} \mathbf{u} \\ \mathbf{v} \end{bmatrix} + \tilde{\omega} \begin{bmatrix} \mathbf{0} & \hat{\mathbf{M}} \\ -\mathbf{1} & \mathbf{0} \end{bmatrix} \begin{bmatrix} \mathbf{u} \\ \mathbf{v} \end{bmatrix} = 0, \quad (22)$$

by introducing $\mathbf{v} \equiv \tilde{\omega} \mathbf{u}$.

The implementation in COMSOL Multiphysics starts by reformulating Eq. (17) into an integral form called the weak formulation. In a weak formulation, as suggested by its name, differential equations are no longer satisfied exactly at every point of the mesh. Instead, they are satisfied in a “weak” sense by considering an overlap integral that involves the multiplication of the equation by certain test (basis) functions. One unique advantage of the weak formulation is that the order of a differential equation can be reduced by using the method of integration by parts to improve numerical stability. Consider Eq. (17) and taking its first-line second-order partial differential equation as an example, we obtain

$$\nabla \times \mu_0^{-1} \nabla \times \tilde{\mathbf{E}} - \tilde{\omega}^2 \varepsilon_\infty \tilde{\mathbf{E}} - \tilde{\omega}^2 \tilde{\mathbf{P}} = 0. \quad (23)$$

The weak formulation of Eq. (23) is derived by introducing a test function denoted by $\tilde{\mathbf{E}}_{\text{test}}$ and evaluating the following overlap integral in the simulation domain Ω ,

$$\int_{\Omega} \tilde{\mathbf{E}}_{\text{test}}(\mathbf{r}) \cdot \nabla \times \mu_0^{-1} \nabla \times \tilde{\mathbf{E}}(\mathbf{r}) - \tilde{\omega}^2 \varepsilon_\infty \tilde{\mathbf{E}}_{\text{test}}(\mathbf{r}) \cdot \tilde{\mathbf{E}}(\mathbf{r}) - \tilde{\omega}^2 \tilde{\mathbf{E}}_{\text{test}}(\mathbf{r}) \cdot \tilde{\mathbf{P}}(\mathbf{r}) d^3 \mathbf{r} = 0. \quad (24)$$

The second-order derivation in Eq. (23) is then reduced to the first order by the technique of integration by parts,

$$\int_{\Omega} \nabla \times \tilde{\mathbf{E}}_{\text{test}}(\mathbf{r}) \cdot \mu_0^{-1} \nabla \times \tilde{\mathbf{E}}(\mathbf{r}) - \tilde{\omega}^2 \varepsilon_\infty \tilde{\mathbf{E}}_{\text{test}}(\mathbf{r}) \cdot \tilde{\mathbf{E}}(\mathbf{r}) - \tilde{\omega}^2 \tilde{\mathbf{E}}_{\text{test}}(\mathbf{r}) \cdot \tilde{\mathbf{P}}(\mathbf{r}) d^3 \mathbf{r} = 0. \quad (25)$$

Here the boundary condition that the electric fields vanish on the outer boundaries of the simulation domain is used. The tutorials of **QNMEig** provide a step-by-step presentation of how to implement the weak formulation using the COMSOL syntax.

5.2 QNM normalization

Normalization enables a direct assessment of the QNM excitation strength α_m used for reconstruction [3]. It is also directly related to one of the main figures of merit of QNM, the field enhancement or the mode volume \tilde{V} , which quantify the interaction strength of the mode with point-like dipoles (molecules): $\tilde{V} \propto \tilde{\mathbf{E}}^{-2}$ (or $\tilde{\mathbf{H}}^{-2}$) for dipolar electric (or magnetic) interactions, $\tilde{\mathbf{E}}$ and $\tilde{\mathbf{H}}$ being the normalized fields. QNM normalization thus represents an essential step in QNM theory.

The literature on QNM normalization, including milestone publications, is quite confusing, sometimes misleading, and not free of mistakes. We refer the reader to Section 4 of the recent review [2], in which the normalization issue has been put into historical perspective and a thorough comparison of all the existing methods has enabled to highlight mistakes and fully clarify the domain of validity. For newcomers, let us mention that the normalization of QNMs (i.e. of open non-Hermitian systems) differs from the classical energy-based norm used for normalizing the normal modes of closed non-Hermitian systems, but no more complicated to implement.

Two markedly different normalization methods are used in **MAN**. Albeit very different in form, they are theoretically equivalent [2,4] and, they are both very easy to implement numerically; they lead to quasi-identical (if the same mesh is used for their computation, >11 common digits are obtained) numerical values, see Fig. 6 in Ref. [2].

The **QNMEig** solver uses the so-called PML-norm [3]. As the name of the method suggests, this norm requires that perfectly matched layers (PMLs) be used to truncate the physical domain and satisfy the outgoing wave condition at the boundary of the computational domain. In practice, the norm $QN = \iiint_{\Omega \cup \Omega_{PML}} \tilde{\mathbf{E}}_m \cdot \frac{\partial \omega \epsilon}{\partial \omega} \tilde{\mathbf{E}}_m - \tilde{\mathbf{H}}_m \cdot \frac{\partial \omega \mu}{\partial \omega} \tilde{\mathbf{H}}_m dV$ is easily computed as a volume integral over the entire computational domain composed of the PML domain Ω_{PML} and the inner physical domain Ω surrounded by the PML. Note that in COMSOL, a complex coordinate stretching is performed inside the PML layer. The PML domain Ω_{PML} , therefore denotes a volume in complex space. In practice, when evaluating the volume integral with real coordinates, one needs to multiply by a Jacobian to accommodate for the change of coordinates: $\iiint_{\Omega_{PML}} \dots dV = \iiint_{V_{PML}} \dots ||\bar{J}|| dV$ with $||\bar{J}||$ the Jacobian, and V_{PML} the volume of the PML layer mapped onto the real coordinates.

The normalization adopted by the **QNMPole** solver does not rely on the calculation of any volume integrals and does not require PMLs. It has been introduced in Ref. [4] and is referred to as the pole-response norm in the literature [2]. It relies on the fact that, for complex frequencies ω sufficiently close to the QNM eigenfrequency $\tilde{\omega}_m$, the scattered field is proportional to the normalized QNM field with a known excitation coefficient: $\lim_{\omega \rightarrow \tilde{\omega}_m} (\omega - \tilde{\omega}_m) \mathbf{E}_s(\mathbf{r}, \omega) = \lim_{\omega \rightarrow \tilde{\omega}_m} (\omega - \tilde{\omega}_m) \alpha_m(\tilde{\omega}_m) \tilde{\mathbf{E}}_m(\mathbf{r})$. As mentioned earlier, there is an infinity of expressions for $\alpha_m(\tilde{\omega}_m)$; however, they all tend towards the same asymptotic expression $\alpha_m(\tilde{\omega}_m)$ as $\omega \rightarrow \tilde{\omega}_m$ and thus the normalization is unique.

The pole-response method is the most general method for QNM normalization: it can be implemented with any frequency-domain Maxwell solvers and can be used for any geometries, including those that cannot accommodate PML boundary conditions, such as photonic-crystal cavities that leak into semi-infinite periodic waveguides [32].

At last, let us emphasize that the basic **QNMEig** and **QNMPole** solvers implemented in **MAN** are dedicated to reciprocal materials for which the right and left QNMs (the left eigenvectors are solutions of the source-free transposed Maxwell operator, see Appendix C in [2]) are identical. For periodic structures (see Section 4.8) or resonators with non-reciprocal materials (see Section 4.6), the right and left eigenvectors are different, and the normalization thus requires performing two independent computations, one for the right QNMs and the other for the left ones. The *nonreciprocal* and *grating* toolboxes are dedicated to these two special cases.

5.3 Completeness of QNM expansion

Completeness refers to the possibility of rigorously reconstructing the field $[\mathbf{E}_S(\mathbf{r}, \omega), \mathbf{H}_S(\mathbf{r}, \omega)]$ scattered by the resonator in the QNM basis, at least for \mathbf{r} belonging to a compact subspace of \mathbb{R}^3 [33-35]. We refer the reader to a recent review [2].

Disappointingly, completeness of expansions involving only true QNMs is rarely met. It is generally admitted that these expansions are complete *only inside the resonators* ($\mathbf{r} \in V_{res}$) and *for resonators in free space* (without substrate), owing to the existence of branch cuts for geometries with a substrate. As explained in [2], there might be hope for future theoretical improvements, but so far, the literature suggests only two possibilities to move towards realistic cases with resonators deposited on substrates, embedded in thin films, or coupled to waveguides.

The first possibility relies on complementing a restricted finite subset of QNMs with another contribution that might be called a non-resonant contribution. Two approaches to compute the non-resonant contribution are available. The first approach, the so-called Riesz projection method [36], relies on computing the non-resonant contribution using a finite-length contour in the complex frequency plane. Alternatively, the non-resonant contribution may also be computed by directly solving Maxwell equations at a few real frequencies, and since it is expected to gently vary with the frequency, it can be easily interpolated [10]. This second approach is implemented in the *interpolation* toolbox described in Section 4.9.

The second possibility, which can be implemented with the **QNMEig** solver approach and the *reconstruction* toolbox, relies on a regularization procedure, initially launched in quantum mechanics, which transforms the open space into a regularized Hilbert space using a complex coordinate transform implemented with perfectly-matched layers [2,3,6,7,15,19]. The spectrum of the regularized operator incorporates true QNMs and numerical modes, which obey the same orthogonality product and, together, admittedly form a complete basis of the regularized ('PMLized') Hilbert space that features square-integrable vectors. A more in-depth discussion can be found in Section 3.4.3 in [2].

State-of-the-art reconstructions of the scattered field by increasing the total number of QNMs and numerical modes retained in the expansion have been obtained with the **QNMEig** solver [6]. The results are quite convincing since convergence is numerically achieved over a broad range of frequencies for complicated geometries: resonators with dispersive materials, resonators lying on dielectric substrates with guiding layers (with branch cuts), nanoresonators on metallic substrates (with branch cuts and accumulation points). In [19], the authors consider simpler geometries, namely 2D cylinders and spheres in free space. They have numerically verified that expansions with QNMs and numerical modes are complete both inside and outside the resonator. They have also verified that expansions based on QNMs only are incomplete everywhere, even inside the resonator, owing to the branch-cut of the Green function in 2D, see Fig. 2 in [19] for more details. The convergence has also been numerically demonstrated in the temporal domain [6]. Another example of converged results is found in Fig. 11 in [7], in which a metal grating with many branch cuts (corresponding to the passing-off of diffraction orders) is analyzed.

5.4 Different methods for reconstruction

Table 3 presents 2×4 methods for reconstructing the total field \mathbf{E}_{tot} . This section qualitatively explains the origin for the existence of various methods.

As the reader may have noted, in Table 3, the analytical expressions for the reconstruction depend on the formula, Eq. (3) or Eq. (4), used to compute the excitation coefficient α_m . This is because we have projected different state vectors onto the QNM basis [19]. The projected state vectors are $[\mathbf{E}_S, \mathbf{H}_S, \mathbf{P}_S, \mathbf{J}_S]^T$ and $[\mathbf{E}_S, \mathbf{H}_S, \mathbf{P}_{tot}, \mathbf{J}_{tot}]^T$ for Eqs. (3) and (4), respectively. Therefore, when adopting Eq. (3), the scattered auxiliary fields can be decomposed into a sum of QNMs, $[\mathbf{P}_S, \mathbf{J}_S] = (\varepsilon(\omega) - \varepsilon_\infty)[\mathbf{E}_S, i\omega\mathbf{E}_S] = \sum_m \alpha_m [\tilde{\mathbf{P}}_m, \tilde{\mathbf{J}}_m]$, whereas, the same formula holds for the total auxiliary fields, $[\mathbf{P}_{tot}, \mathbf{J}_{tot}] = (\varepsilon(\omega) - \varepsilon_\infty)[\mathbf{E}_{tot}, i\omega\mathbf{E}_{tot}] = \sum_m \alpha_m [\tilde{\mathbf{P}}_m, \tilde{\mathbf{J}}_m]$, when adopting Eq. (4).

Let us now explain how the method **M 4** is obtained. Let us start by reconstructing the total magnetic field with the simplest formula, $\mathbf{H}_{tot} = \sum_m \alpha_m \tilde{\mathbf{H}}_m + \mathbf{H}_b$. Then we use the Maxwell equation, $\mathbf{E}_{tot} = [i\omega\epsilon(\omega)]^{-1}\nabla \times \mathbf{H}_{tot}$, to deduce the \mathbf{E}_{tot} (method **M 4** in Table 3). Indeed, when all the QNMs are retained in the expansion, the \mathbf{E}_{tot} expressions of methods **M 4** and **M 1** ($\mathbf{E}_{tot} = \sum_m \alpha_m \tilde{\mathbf{E}}_m + \mathbf{E}_b$) are mathematically equivalent; however, when truncating the series, they differ. Likewise, for dispersive resonators, \mathbf{E}_{tot} can also be deduced from the reconstructed auxiliary fields \mathbf{P}_{tot} and \mathbf{J}_{tot} , therein leading to methods **M 2** and **M 3**.

It is natural to wonder which reconstruction method provides the most accurate prediction by retaining the smallest number of QNMs in the expansion. According to our experience, there is no general answer to that question. When reconstructing the fields for plasmonic resonators [8] and high-index dielectric Mie nanoresonators [9], we have observed that the accuracies achieved with methods **M 2**, **M 3**, **M 4** are comparable when considering dozens of QNMs. Methods **M 3** and **M 4** may have a slightly slower convergence for high-index nanoresonators, possibly because the contribution of numerous high-frequency modes is boosted with the prefactor $\tilde{\omega}_m/\omega$.

On the other hand, we have observed that the simplest and most widespread reconstruction method **M 1** ($[\mathbf{E}_{tot}, \mathbf{H}_{tot}] = \sum_m \alpha_m [\tilde{\mathbf{E}}_m, \tilde{\mathbf{H}}_m] + [\mathbf{E}_b, \mathbf{H}_b]$) is rarely capable of providing very accurate reconstructions (an example is provided in Fig. 4), except for some simple cases for which the optical response can be fully described with 1 or 2 dominant QNMs [3,4]. The reason can be intuitively understood. Consider the reconstruction of the total electric field of a non-dispersive resonator and imagine that the resonator is illuminated by a plane wave. The continuity of the normal component of the electric displacement field across the boundary of the resonator $\mathbf{n} \cdot \mathbf{D}_{tot+} = \mathbf{n} \cdot \mathbf{D}_{tot-}$ has to be fulfilled. However, since the background electric field \mathbf{E}_b is a continuous function across the boundary of the resonator, the reconstruction with ‘transverse’ QNMs satisfying $\mathbf{n} \cdot \tilde{\mathbf{D}}_{m+} = \mathbf{n} \cdot \tilde{\mathbf{D}}_{m-}$ naturally results in a discontinuity $\mathbf{n} \cdot (\epsilon_+ \mathbf{E}_{b+} - \epsilon_- \mathbf{E}_{b-})$ of the normal component of the electric displacement, which can only be compensated by the contribution of a large set of longitudinal QNMs satisfying $\mathbf{n} \cdot \tilde{\mathbf{D}}_{m+} \neq \mathbf{n} \cdot \tilde{\mathbf{D}}_{m-}$. These longitudinal QNMs satisfy the source-free Maxwell equations at zero frequency, $\nabla \times \tilde{\mathbf{E}}_m = 0$, and are called electric static QNMs [18,37] in the literature. We have not yet understood for which geometry their contribution is significant or negligible. However, if their contribution cannot be neglected, they may require to compute a large number of numerical electrostatic-like modes with complex frequencies close to the zero frequency. In a few occasions, we have also computed them with the electrostatic solver of COMSOL [38]. Note that the contribution of the electrostatic-like modes is a smooth function of the frequency in the visible and that it is easily taken into account with the *interpolation* toolbox.

5.5 Symmetry

Mirror Symmetry. Many optical resonators exhibit mirror symmetry, i.e. the resonator can be superimposed with itself by flipping it with respect to one or several planes. It is beneficial to implement perfect electric/magnetic conductors (PEC/PMC) at the symmetry planes and only mesh one-half, one-quarter, or even one-eighth of the systems, to speed up the QNMs computation by approximately one order of magnitude in 3D. Depending on whether the implemented boundary condition at the symmetry plane is PMC or PEC, QNMs with the specific mirror symmetry will be computed. For example, for a PEC in the x - y plane, only the QNM with $[\tilde{E}_x(\mathbf{r}), \tilde{E}_y(\mathbf{r}), \tilde{E}_z(\mathbf{r})] = [-\tilde{E}_x(\mathbf{r}'), -\tilde{E}_y(\mathbf{r}'), \tilde{E}_z(\mathbf{r}')]$, with $\mathbf{r} = [x, y, z]$ and $\mathbf{r}' = [x, y, -z]$, will be computed in the upper half-space ($z > 0$). **MAN** includes built-in functions to automatically derive the QNM fields in the unmeshed space, in such case the lower half-space ($z < 0$).

Axisymmetry. 3D axisymmetric optical nanoresonators are widely experienced in nanophotonics. Typical examples include whispering gallery resonators, spherical dimers, nanodisks, and so on. The QNM computation for these geometries can be simplified to a 2D problem by implementing axial

symmetry. The average time for computing one QNM can be reduced by a few orders of magnitude, and numerical stability can be greatly enhanced.

In the cylindrical coordinate system $\{\rho, \phi, z\}$, the axisymmetric QNM fields can be expressed as

$$\tilde{\mathbf{E}}_m(\mathbf{r}) = \tilde{\mathbf{e}}_m(\rho, z) \exp(im\phi), \text{ and } \tilde{\mathbf{H}}_m(\mathbf{r}) = \tilde{\mathbf{h}}_m(\rho, z) \exp(im\phi), \quad (26)$$

where $m = 0, \pm 1, \pm 2, \dots$ denotes the azimuthal order of the mode. The azimuthal dependence of the fields $\exp(im\phi)$ being explicit, the determination of $\tilde{\mathbf{e}}_m(\rho, z)$ and $\tilde{\mathbf{h}}_m(\rho, z)$ corresponds to a 2D problem since only two variables, ρ and z , are involved. The COMSOL model QNMEig_axi_NPoM.mph illustrates how to implement the axial symmetry for metal nanocylinders on a metal substrate (NPoM) or on a hybrid nanostructure consisting of a 2D material and a plasmonic nanoantenna. They may help the user to develop their own models.

For reciprocal systems, i.e., $\boldsymbol{\mu} = \boldsymbol{\mu}^T$ or $\boldsymbol{\epsilon} = \boldsymbol{\epsilon}^T$, the normalization of axisymmetric QNMs involves $\{\tilde{\mathbf{e}}_m(\rho, z), \tilde{\mathbf{h}}_m(\rho, z)\}$ and $\{\tilde{\mathbf{e}}_{-m}(\rho, z), \tilde{\mathbf{h}}_{-m}(\rho, z)\}$

$$QN = 2\pi \iint_{\Omega \cup \Omega_{\text{PML}}} \rho \left(\tilde{\mathbf{e}}_{-m} \cdot \frac{\partial(\omega\boldsymbol{\epsilon})}{\partial\omega} \tilde{\mathbf{e}}_m - \tilde{\mathbf{h}}_{-m} \cdot \frac{\partial(\omega\boldsymbol{\mu})}{\partial\omega} \tilde{\mathbf{h}}_m \right) d\rho dz. \quad (27)$$

However since $\{\tilde{\mathbf{e}}_m(\rho, z), \tilde{\mathbf{h}}_m(\rho, z)\}$ can be directly deduced from $\{\tilde{\mathbf{e}}_{-m}(\rho, z), \tilde{\mathbf{h}}_{-m}(\rho, z)\}$, $\tilde{\mathbf{e}}_m \cdot \hat{\rho} = \tilde{\mathbf{e}}_{-m} \cdot \hat{\rho}$, $\tilde{\mathbf{e}}_m \cdot \hat{z} = \tilde{\mathbf{e}}_{-m} \cdot \hat{z}$, $\tilde{\mathbf{e}}_m \cdot \hat{\phi} = -\tilde{\mathbf{e}}_{-m} \cdot \hat{\phi}$, $\tilde{\mathbf{h}}_m \cdot \hat{\rho} = -\tilde{\mathbf{h}}_{-m} \cdot \hat{\rho}$, $\tilde{\mathbf{h}}_m \cdot \hat{z} = -\tilde{\mathbf{h}}_{-m} \cdot \hat{z}$, and $\tilde{\mathbf{h}}_m \cdot \hat{\phi} = \tilde{\mathbf{h}}_{-m} \cdot \hat{\phi}$, QN can be calculated with a single QNM computation.

6. Conclusion

We have introduced **MAN**, an open-source MATLAB program to model light scattering by electromagnetic resonators based on quasinormal-mode expansions. The manuscript provides an overview of the possibilities offered by the software and references the key formulas implemented in the program. **MAN** also includes a comprehensive suite of self-contained geometry examples to illustrate the program's capabilities for realistic calculations and various emblematic resonators in modern photonics. We hope this program will be useful to the nanophotonics community, and we welcome contributions to extend the program use cases.

MAN gathers two QNM solvers, **QNMPole** and **QNMEig**, which have already acquired a good reputation as can be seen from the number of citations of the referent publications [3,4,6] or software downloads [21]. **QNMEig** provides a comprehensive interface to the commercial software COMSOL Multiphysics; **QNMPole** can be used with any software capable of solving Maxwell equations in the frequency domain. The solvers are completely different, and together, they cover a broad scope of applications in nanophotonics and quantum optics, as illustrated by the increasing number of toolboxes incorporated in the software.

The present version achieves a major shift in the development of the software. We conclude below with a summary of the main new features:

- Unified use of the **QNMEig** and **QNMPole** solvers
- *User-friendly TUTORIALS* scripts that provide a step-by-step illustration of how to compute, normalize, sort, and visualize QNMs with both QNM solvers
- Export of QNM fields in any user-defined coordinates
- A set of built-in functions that provide direct access to important QNM figures of merit, e.g. mode volume, brightness, radiation diagram, multipolar content
- A dedicated toolbox for reconstructing the scattered field in the QNM basis
- An extended set of COMSOL models encompassing a great variety of nanophotonic devices
- Additional built-in material dielectric functions

Overall, we expect that the new version is much more didactical and will assist the user to develop their own applications.

Acknowledgment

The authors acknowledge the help of Marc Duruflé (INRIA Bordeaux), Rémi Faggiani (Greenerwave), Jianji Yang (Meta/FRL), Alexandre Gras, Carlo Gigli (EPFL), Qiang Bai, Mondher Besbes, Jean-Paul Hugonin and Christophe Sauvan.

Data Availability

Data underlying the results presented in this paper are not publicly available at this time but may be obtained from the authors upon reasonable request.

Declaration of Competing Interest

The authors declare that they have no known competing financial interests or personal relationships that could have appeared to influence the work reported in this paper.

References

1. P. Lalanne, W. Yan, V. Kevin, C. Sauvan, J.-P. Hugonin, *Laser Photon. Rev.* 12 (2018) 1700113.
2. C. Sauvan, T. Wu, R. Zarouf, E. A. Muljarov, P. Lalanne, *Opt. Express* 30 (2022) 6846.
3. C. Sauvan, J.-P. Hugonin, I.S. Maksymov, P. Lalanne, *Phys. Rev. Lett.* 110 (2013) 237401.
4. Q. Bai, M. Perrin, C. Sauvan, J.-P. Hugonin, P. Lalanne, *Opt. Express* 21 (2013) 27371.
5. R. Faggiani, A. Losquin, J. Yang, E. Mårsell, A. Mikkelsen, P. Lalanne, *ACS Photonics* 4 (2017) 897.
6. W. Yan, R. Faggiani, P. Lalanne, *Phys. Rev. B* 97 (2018) 205422.
7. A. Gras, W. Yan, P. Lalanne, *Opt. Lett.* 44 (2019) 3494.
8. T. Wu, A. Baron, P. Lalanne, K. Vynck, *Phys. Rev. A* 101 (2020) 011803(R).
9. C. Gigli, T. Wu, G. Marino, A. Borne, G. Leo, P. Lalanne, *ACS Photonics* 7 (2020) 1197.
10. T. Wu, D. Arrivault, M. Duruflé, A. Gras, F. Binkowski, S. Burger, W. Yan, P. Lalanne, *J. Opt. Soc. Am. A* 38 (2021) 1224.
11. T. Wu, M. Gurioli, P. Lalanne, *ACS Photonics* 8 (2021) 1522.
12. T. Wu, P. Lalanne, *arXiv:2106.05502* (2021).
13. E. A. Muljarov, W. Langbein, *Phys. Rev. B* 93 (2016) 075417.
14. W. C. Chew, W. H. Weedon, *Microwave Opt. Technol. Lett.* 7 (1994) 599.
15. B. Vial, A. Nicolet, F. Zolla, M. Commandré, *Phys. Rev. A* 89 (2014) 023829.
16. J. Yang, J.-P. Hugonin, P. Lalanne, *ACS Photonics* 3 (2016) 395.
17. M. D. Truong, A. Nicolet, G. Demésy, F. Zolla, *Opt. Express* 28 (2020) 29016.
18. C. Sauvan, *Opt. Express* 29 (2021) 8268.
19. A. Gras, P. Lalanne, M. Duruflé, *J. Opt. Soc. Am. A* 37 (2020) 1219.
20. M. P. Fischer, N. Maccaferri, K. Gallacher, J. Frigerio, G. Pellegrini, D. J. Paul, G. Isella, A. Leitenstorfer, P. Biagioni, D. Brida, *Optica* 8 (2021) 898.
21. <https://www.lp2n.institutoptique.fr/equipes-de-recherche-du-lp2n/light-complex-nanostructures>
22. F. Binkowski, F. Betz, R. Colom, M. Hammerschmidt, L. Zschiedrich, S. Burger, *Phys. Rev. B* 102 (2020) 035432.
23. R. Alaee, C. Rockstuhl, I. Fernandez-Corbaton, *Adv. Opt. Mater* 7 (2019) 1800783.
24. W. Liu, Y. Kivshar, *Opt. Express* 26 (2018) 13085.
25. P. D. Terekhov, K. V. Baryshnikova, Y. A. Artemyev, A. Karabchevsky, A. S. Shalin, A. B. Evlyukhin, *Phys. Rev. B* 96 (2017) 035443.
26. F. Zolla, A. Nicolet, G. Demésy, *Opt. Lett.* 43 (2018) 5813.
27. B. Vial, G. Demésy, F. Zolla, A. Nicolet, M. Commandré, C. Hecquet, T. Begou, S. Tisserand, S. Gautier, V. Sauget, *J. Opt. Soc. Am. B* 31 (2014) 1339.
28. P. Lalanne, G. M. Morris, *J. Opt. Soc. Am. A* 13 (1996) 779.

29. A. Raman, S. Fan, Phys. Rev. Lett. 104 (2010) 087401.
30. A. Taflove, S.G. Johnson, A. Oskooi, (Artech House, Boston, Mass., 2013). "Advances in FDTD Computational Electrodynamics: Photonics and Nanotechnology"
31. J. Zimmerling, L. Wei, P. Urbach, R. Remis, J. Comput. Phys. 315 (2016) 348.
32. R. Faggiani, J. Yang, R. Hostein, P. Lalanne, Optica 4 (2017) 393.
33. R. M. More, Phys. Rev. A 4 (1971) 1782.
34. [C. E. Baum, Interaction Note 88, December 1971. See <https://apps.dtic.mil/sti/citations/ADA066905>
35. P. T. Leung, S. Y. Liu, K. Young, Phys. Rev. A 49 (1994) 3057.
36. L. Zschiedrich, F. Binkowski, N. Nikolay, O. Benson, G. Kewes, S. Burger, Phys. Rev. A 98 (2018) 043806.
37. M. B. Doost, W. Langbein, E. A. Muljarov, Phys. Rev. A 90 (2014) 013834.
38. W. Yan, P. Lalanne, M. Qiu, Phys. Rev. Lett. 125 (2020) 013901.